Available online at www.sciencedirect.com
ScienceDirect
Comput. Methods Appl. Mech. Engrg. 386 (2021) 114101
Computer methods in applied mechanics and engineering
www.elsevier.com/locate/cma

A Nitsche stabilized finite element method: Application for heat and mass transfer and fluid–structure interaction

Bin Liu

Department of Mechanical Engineering, National University of Singapore, Singapore, 119077, Singapore

Received 21 January 2021; received in revised form 18 June 2021; accepted 8 August 2021
Available online 1 September 2021

Abstract

A Nitsche stabilized finite element method is proposed for heat & mass transfer and fluid–structure interaction. The GLS/PSPG stabilization is employed to stabilize the finite element formulation. The Nitsche's methods are employed to weakly impose the Dirichlet condition for heat & mass transfer. An upwind term is included in Nitsche's methods to enhance the stability for fast moving interfaces. The Ghost penalty method is employed to control the jumps across the cut cells. The projection-based adaptive Gauss quadrature (PAGQ) scheme is used for the numerical integration of the discontinuous function. The nonlinear advection–diffusion equations are linearized by Newton procedure. The second-order accurate unconditionally stable generalized-α time integration is implemented to march the solution in time. The fluid and the structure equations are weakly coupled by a second-order accurate staggered-partitioned scheme. Numerical examples include the cases of fixed/vibrating/rotating cylinder(s) for heat & mass transfer and fluid–structure interaction in enclosure and external flow. The obtained numerical results match well with the experiments, the empirical correlation and the numerical simulations in literature. This methodology efficiently and accurately simulates the complex physics of heat & mass transfer.

Keywords: Nitsche's method; GLS/PSPG stabilization; Ghost penalty method; Projection-based adaptive gauss quadrature; Heat & mass transfer; Fluid–structure interaction

1. Introduction

Numerical simulations of the complex heat & mass transfer and the fluid–structure interaction are the challenging tasks, because of the numerous difficulties associated with the geometrical and the physical characteristics of the multi-physics and the multi-scale phenomena. The subtle and fascinating coupling phenomenon between the fluid, the structure and the heat & mass transfer has attracted attention across diverse research communities. Especially, the heat & mass transfer and the fluid–structure interaction naturally occur in many bio-related research, e.g., hemodynamics & blood cells circulation, respiratory system, waste water treatment and colloidal systems, and various engineering applications, e.g., evaporators & heat exchanger, nuclear power plant, solar desalination farm and hydrogen fuel cells. To address these physics-rich and challenging topics, where the large structural displacements, the complicated structural deformations and the subtle interaction of heat & mass transfer are frequently observed, we propose an accurate and robust numerical formulation based on the Nitsche's methods and the unfitted stabilized finite element method.

E-mail address: a0098961@u.nus.edu.

https://doi.org/10.1016/j.cma.2021.114101
0045-7825/

Nomenclature

Fluid variables

Re	Reynolds number ($\frac{U_\infty L}{\nu}$)
Gr	Grashof number ($\frac{g\beta_t(T_h-T_l)L^3}{\nu^2}$)
Pr	Prandtl number ($\frac{\nu}{\alpha}$)
Ra	Thermal Rayleigh number ($\frac{g\beta_t(T_h-T_l)L^3}{\alpha\nu} = GrPr$)
ν	Kinematic viscosity
Ri	Richardson number ($\frac{Gr}{Re^2}$)
Le	Lewis number ($\frac{\alpha}{D}$)
Br	Buoyancy ratio ($\frac{\beta_c(c_h-c_l)}{\beta_t(T_h-T_l)}$)
β_t	Thermal expansion coefficient
β_c	Compositional expansion coefficient
U_∞	Freestream velocity
ρ	Fluid density
ρ_0	Referential fluid density
$\boldsymbol{g}$	Gravitational acceleration vector
$\boldsymbol{u}$	Fluid velocity vector
$\boldsymbol{u}^*$	Dimensionless fluid velocity vector
p	Fluid pressure
p^*	Dimensionless pressure
$\boldsymbol{h}$	Surface traction vector
c_p	Constant pressure specific heat
α	Thermal diffusivity
D	Species diffusivity
T	Temperature
θ	Dimensionless temperature
q	Surface heat flux
c	Concentration of species
C	Dimensionless concentration of species
j	Surface species flux

Structure variables

L	Characteristic length
m^*	Mass ratio ($\frac{m^s}{0.25\pi L^2\rho_0}$)
ζ	Damping ratio
a	Angular velocity
Ur	Reduced velocity ($\frac{U_\infty}{f_{ny}L}$)
$\boldsymbol{f}_n$	Structural frequency vector ($[f_{nx}, f_{ny}]'$)
$\boldsymbol{\Phi}^*$	Dimensionless location of structure
$\boldsymbol{\eta}^*$	Dimensionless displacement of structure
DoF	Degree-of-Freedom of vibration

Post-processing quantities

Nu	Averaged Nusselt number ($-\frac{1}{\pi L}\int_0^{\pi L}\frac{\partial\theta}{\partial\boldsymbol{n}}ds$)
Sh	Averaged Sherwood number ($-\frac{1}{\pi L}\int_0^{\pi L}\frac{\partial C}{\partial\boldsymbol{n}}ds$) .

Cd	Drag coefficient
Cl	Lift coefficient
A_x	Streamwise vibration amplitude
A_y	Transverse vibration amplitude
St	Strouhal number
f_{vs}	Vortex-shedding frequency
ω	Spanwise vorticity
τ	Dimensionless time

Superscripts

$*$	Dimensionless quantity
f	Fluid quantity
s	Structural quantity
fs	Fluid–structure interface
cyl	Cylinder
$'$	Transpose operator

Subscripts

vs	Vortex shedding
h	High
l	Low
t	Temperature
c	Species

The unfitted formulation is an appealing approach to simulate the physical situations where the large structural deformation and displacement are observed, e.g., fluid–structure interaction, membrane or free surface flows. In this family of methods, the fluid is modeled in the (spatial) Eulerian frame of reference while the immersed structure is described in the Lagrangian frame of reference. The advantage is that the fluid grid does not have to align with the fluid–structure interface. Therefore, the additional efforts of generating body-fitted meshes and complex re-meshing algorithms for dealing with large-structural deformation are completely avoided. However, because of the fluid–structure interface is not aligned, it results in an embedded discontinuity within the finite elements and imposes challenges to the numerical formulations. To this end, the specialized techniques are employed to weakly enforce the boundary conditions along an embedded interface and optimize the numerical integration over the discontinuous functions. For example, the immersed boundary (IB) method [1,2] and its variations, e.g., [3–7], are the ones among the well-accepted approaches in *unfitted* formulation. Alternative well-established numerical methods under finite element framework are the distributed Lagrange multiplier/fictitious domain (DLM/FD) methods [8–10] and the extended finite element methods [11–13].

The idea of distributing the Lagrange points along an embedded interface was well established in the IB and DLM/FD methods. However, the usage of the Lagrangian multipliers increases the overall size of system matrix. Furthermore, an appropriate choice of Lagrange multiplier basis space is critical to satisfy the Babŭska–Brezzi (BB) condition [14,15]. Subsequently, the Nitsche's methods gained attention among the research communities and is actively developed, because of its advantages, e.g., variational consistency and no increment of system size (no explicit introduction of Lagrangian multipliers). Nitsche's method was first proposed in Nitsche (1971) [16]. Recently, a number of variances of Nitsche's methods were proposed to solve different problems. For instance, Burman (2010) [17] proposed a robust stabilization technique (Ghost penalty method) for the fictitious domain methods and subsequently applied it for the Nitsche's methods. Burman (2012) [18] and Schillinger et al. (2016) [19] documented the penalty-free non-symmetric Nitsche's method. Bazilevs et al. (2012) [20] introduced an upwind term to enhance the stability of Nitsche's methods in case of a fast moving interface. Massing et al. (2014) [21] formulated the Nitsche's method for Stokes problem. Nguyen et al. (2017) [22] proposed a diffuse Nitsche's method

for the applications with phase-field boundaries, e.g., free-surface waves and multi-phase flow. Zou et al. (2017) [23] proposed a Nitsche's method for Helmholtz problems. Liu & Tan (2020) [24] derived a numerical integration scheme to deal with the discontinuous function within the finite elements, the projection-based adaptive Gauss quadrature (PAGQ) scheme, and applied it for Nitsche's methods. In addition, the various Nitsche's methods have been widely used in the simulations of fluid–structure interaction (FSI) problems, e.g., [25–28]. In this article, a Nitsche's method formulation is proposed for the simulations of heat & mass transfer and fluid–structure interaction.

Compared with the fluid–structure interaction problems in the isothermal fluid flow, the rich physics induced by the subtle interaction between fluid, structure, temperature and species field in wake is phenomenal. Recently, a number of novel numerical formulations of embedded interface are proposed for heat transfer in fluid flow [29,30]. In this article, we consider not only heat transfer, but mass transfer, fluid–structure interaction and their complicated triple coupling. To this end, a robust Nitsche stabilized finite element formulation for multi-component and multi-physics simulations involving large structural displacement, heat convection, thermal buoyancy, suspension of different-density species is proposed in this article. The characteristics of the proposed formulation are listed below

- Nitsche's method for heat & mass transfer and fluid–structure interaction
- Projected-based adaptive Gauss quadrature (PAGQ) [24] scheme for numerical integration of discontinuous function over embedded interface with heat & mass transfer
- Ghost penalty method [17] stabilizing the jumps over the embedded interface in heat & mass transfer
- GLS/PSPG [31,32] stabilization and the outflow correction [33] for heat & mass transfer and fluid–structure interaction
- An upwind term [20] to stabilize the Ntische's method in case of fast moving interface
- Second-order accurate unconditionally stable generalized-α time integration for both fluid and structure equations
- Second-order accurate staggered-partitioned weakly-coupling fluids–structure interaction schemes for heat & mass transfer.

This article is organized as follows: In Section 2, the governing equations are presented, which consist of the unsteady Navier–Stokes equation and the conservation of energy and species. The stabilized Nitsche finite element formulation for heat & mass transfer and fluid–structure interaction is proposed in Section 3. The numerical integration scheme, the time integration schemes and the fluid–structure coupling schemes are derived in Section 3 as well. Subsequently, the numerical examples are presented in Section 4 to validate the proposed numerical formulation. Finally, the concluding remarks are shown in Section 5.

2. Governing equations

The governing equations consist of the unsteady incompressible Navier–Stokes equation, the conservation of energy and the conservation of species. The conservation of energy and species are coupled with the conservation of momentum (Navier–Stokes equation) via Boussinesq Approximation. The coupled governing equations are subsequently non-dimensionalized by a set of dimensionless groups. This set of dimensionless groups is frequently used for the problems of external flow, where the free-stream velocity is normally known. In double-diffusive mixed convective flow, both the conservation of energy and species are coupled with the Navier–Stokes equation. For either the heat or the mass transfer problem, the conservation of species or energy can be simply decoupled with the Navier–Stokes equation.

2.1. Navier–Stokes Equation

The unsteady incompressible Navier–Stokes equation is presented in Eq. (1), where $\boldsymbol{u}$, p and ρ respectively are the fluid velocity vector, the pressure and the density. $\boldsymbol{g} = [0, -g]' = [0, -9.81]'$ is the gravitational acceleration vector, where the superscript $(\cdot)'$ is a transpose operator. The operator $\partial_t(\cdot)$ refers to the temporal derivative of a variable. $\tilde{\boldsymbol{u}}$ and $\tilde{h}$ are the prescribed fluid velocity and the surface traction along the Dirichlet (Γ_D^f) and the Neumann (Γ_N^f) boundaries respectively, where they are complementary subsets of the entire fluid-domain boundaries Γ^f

($\Gamma^f \cup \Gamma^f_N = \Gamma^f$ and $\Gamma^f_D \cap \Gamma^f_N = \emptyset$). The superscript f indicates the quantities of the fluid domain. $\tilde{\boldsymbol{u}}_0$ is the prescribed initial fluid velocity, and $\boldsymbol{n}$ is an outward normal vector.

$$\nabla \cdot \boldsymbol{u} = 0 \qquad \forall \boldsymbol{x} \in \Omega^f(t) \tag{1a}$$

$$\rho\big(\partial_t \boldsymbol{u} + (\boldsymbol{u} \cdot \nabla)\boldsymbol{u}\big) = -\nabla p + \mu \nabla^2 \boldsymbol{u} + \rho \boldsymbol{g} \qquad \forall \boldsymbol{x} \in \Omega^f(t) \tag{1b}$$

$$\boldsymbol{u} = \tilde{\boldsymbol{u}} \qquad \forall \boldsymbol{x} \in \Gamma^f_D(t) \tag{1c}$$

$$\boldsymbol{\sigma}\{\boldsymbol{u}, p\} \cdot \boldsymbol{n} = \tilde{\boldsymbol{h}} \qquad \forall \boldsymbol{x} \in \Gamma^f_N(t) \tag{1d}$$

$$\boldsymbol{u} = \tilde{\boldsymbol{u}}_0 \qquad \forall \boldsymbol{x} \in \Omega^f(0) \tag{1e}$$

The Cauchy stress tensor ($\boldsymbol{\sigma}$) for incompressible Newtonian fluid is defined as

$$\boldsymbol{\sigma}\{\boldsymbol{u}, p\} = -p\boldsymbol{I} + 2\mu\epsilon(\boldsymbol{u}) \tag{2a}$$

$$\epsilon(\boldsymbol{u}) = \frac{1}{2}\Big[\nabla \boldsymbol{u} + (\nabla \boldsymbol{u})'\Big] \tag{2b}$$

where $\boldsymbol{I}$, μ and $\epsilon(\boldsymbol{u})$ respectively are the identity matrix, the dynamic viscosity and the strain rate tensor.

2.2. Heat and mass transfer

The dynamics and the stability of heat & mass transfer are governed by the conservation of energy and species in Eqs. (3a) and (3b), where T and c respectively refer to the temperature of fluid and the concentration of species. The value of α in Eq. (3a) is the thermal diffusivity; and D in Eq. (3b) is the species diffusivity.

$$\partial_t T + (\boldsymbol{u} \cdot \nabla)T = \alpha \nabla^2 T \qquad \forall \boldsymbol{x} \in \Omega^f(t) \tag{3a}$$

$$\partial_t c + (\boldsymbol{u} \cdot \nabla)c = D \nabla^2 c \qquad \forall \boldsymbol{x} \in \Omega^f(t) \tag{3b}$$

$$T = \tilde{T};\ c = \tilde{c} \qquad \forall \boldsymbol{x} \in \Gamma^f_D(t) \tag{3c}$$

$$\alpha(\nabla T) \cdot \boldsymbol{n} = \tilde{q};\ D(\nabla c) \cdot \boldsymbol{n} = \tilde{j} \qquad \forall \boldsymbol{x} \in \Gamma^f_N(t) \tag{3d}$$

$$T = \tilde{T}_0;\ c = \tilde{c}_0 \qquad \forall \boldsymbol{x} \in \Omega^f(0) \tag{3e}$$

$\tilde{T}$, $\tilde{c}$, $\tilde{q}$ and $\tilde{j}$ respectively are the prescribed temperature, the prescribed concentration of species, the prescribed heat flux and the prescribed species flux along the boundaries of fluid domain. $\tilde{T}_0$ and $\tilde{c}_0$ are the initial conditions of the temperature and the species concentration.

For double diffusive heat & mass transfer in fluid, Eqs. (1a), (1b), (3a) and (3b) are solved together. If the fluid inertia is dominant, e.g., the forced convection, the influence of the temperature and the species concentration on the fluid inertia can be neglected. In such cases, the coupling between the Navier–Stokes equation and the conservation of energy and species are unilateral. In other words, the heat and species convection are driven by the fluid velocity, the convection terms ($\boldsymbol{u}\cdot(\cdot)$) on the left-hand side of Eqs. (3a) and (3b); whereas the Navier–Stokes equation remains unchanged. On the other hand, if the dynamics of heat & mass transfer are comparable to the fluid inertia, e.g., the mixed or natural convection, the coupling becomes bilateral instead, due to the changes in fluid density induced by the gradients of temperature (buoyancy action) and species concentration. Because of the small density variations present in these type of flows, a general incompressible flow approximation is normally adopted. Assuming the density is a function of temperature, $\rho = \rho(T, c)$, the elementary thermodynamics states that $\beta_t = -\frac{1}{\rho_0}(\partial\rho/\partial T)_c$ and $\beta_c = -\frac{1}{\rho_0}(\partial\rho/\partial c)_t$. Hence the density of fluid depends on both temperature and species concentration, which can be written as

$$\rho = \rho_0\big[1.0 - \beta_t(T - T_l) - \beta_c(c - c_l)\big] \tag{4}$$

where ρ_0 is the referential fluid density. These considerations lead to the Boussinesq Approximation and result in a force term ($\rho\boldsymbol{g}$) added in the y-component of Navier–Stokes equation. Since there is a referential fluid velocity (U_∞) in this study, the following dimensionless groups in Eq. (5) are used to non-dimensionalize the full set of coupled equations. The resultant dimensionless form is presented in Eq. (6), where the Navier–Stokes equation is converted to its conservative form by substituting the conservation of mass. $\boldsymbol{n}_g = [0, -1.0]'$ is the unit vector of

gravitational force. Re, Pr, Le and Br refer to the Reynolds number, the Prandtl number, the Lewis number and the buoyancy ratio respectively. They are defined in Eq. (7), where Gr is the Grashof number.

$$\boldsymbol{x}^* = \frac{\boldsymbol{x}}{L}; \quad \boldsymbol{u}^* = \frac{\boldsymbol{u}}{U_\infty}; \quad \tau = \frac{tU_\infty}{D} \tag{5a}$$

$$p^* = \frac{p + \rho_0 g z}{\rho_0 U_\infty^2}; \quad \theta = \frac{T - T_l}{T_h - T_l}; \quad C = \frac{c - c_l}{c_h - c_l} \tag{5b}$$

$$\nabla \cdot \boldsymbol{u}^* = 0 \qquad \forall \boldsymbol{x}^* \in \Omega^f(\tau) \tag{6a}$$

$$\partial_\tau \boldsymbol{u}^* + (\boldsymbol{u}^* \cdot \nabla)\boldsymbol{u}^* = -\nabla p^* + \frac{1}{Re}\nabla \cdot \left(\nabla \boldsymbol{u}^* + (\nabla \boldsymbol{u}^*)'\right) - (Ri\ \boldsymbol{n}_g)(\theta + Br\ C) \qquad \forall \boldsymbol{x}^* \in \Omega^f(\tau) \tag{6b}$$

$$\partial_\tau \theta + (\boldsymbol{u}^* \cdot \nabla)\theta = \frac{1}{Re\ Pr}\nabla^2 \theta \qquad \forall \boldsymbol{x}^* \in \Omega^f(\tau) \tag{6c}$$

$$\partial_\tau C + (\boldsymbol{u}^* \cdot \nabla)C = \frac{1}{Le\ Re\ Pr}\nabla^2 C \qquad \forall \boldsymbol{x}^* \in \Omega^f(\tau) \tag{6d}$$

$$\boldsymbol{u}^* = \tilde{\boldsymbol{u}}^*; \quad \theta = \tilde{\theta}; \quad C = \tilde{C} \qquad \forall \boldsymbol{x}^* \in \Gamma_D^f(\tau) \tag{6e}$$

$$\left(-p^* \boldsymbol{I} + \frac{2}{Re}\epsilon(\boldsymbol{u}^*)\right) \cdot \boldsymbol{n} = \tilde{\boldsymbol{h}}^*; \quad \left(\frac{1}{Re\ Pr}\nabla\theta\right) \cdot \boldsymbol{n} = \tilde{q}^*; \quad \left(\frac{1}{Le\ Re\ Pr}\nabla C\right) \cdot \boldsymbol{n} = \tilde{j}^* \qquad \forall \boldsymbol{x}^* \in \Gamma_N^f(\tau) \tag{6f}$$

$$\boldsymbol{u}^* = \tilde{\boldsymbol{u}}_0^*; \quad \theta = \tilde{\theta}_0; \quad C = \tilde{C}_0 \qquad \forall \boldsymbol{x}^* \in \Omega^f(0) \tag{6g}$$

$$Re = \frac{U_\infty L}{\nu}; \quad Ri = \frac{g\beta_t(T_h - T_l)L}{U_\infty^2} = \frac{Gr}{Re^2}; \quad Br = \frac{\beta_c(c_h - c_l)}{\beta_t(T_h - T_l)} \tag{7a}$$

$$Pr = \frac{\nu}{\alpha}; \quad Gr = \frac{g\beta_t(T_h - T_l)L^3}{\nu^2}; \quad Le = \frac{\alpha}{D} \tag{7b}$$

In Eqs. (5) and (6), the superscript $(*)$ means the quantity is dimensionless. The subscripts (h and l) represent the highest and lowest temperature and species concentration in the computational domain. τ and θ respectively are the dimensionless time and the dimensionless temperature. The value of z is the elevation height in the direction of gravitational acceleration. L refers to the characteristic length, e.g., the diameter of a cylinder or the length of an enclosure. The averaged Nusselt number (Nu) and Sherwood number (Sh) around the surface of cylinder (diameter L) can be computed as.

$$Nu = -\frac{1}{\pi L}\int_0^{\pi L} \frac{\partial \theta}{\partial \boldsymbol{n}} ds; \quad Sh = -\frac{1}{\pi L}\int_0^{\pi L} \frac{\partial C}{\partial \boldsymbol{n}} ds \tag{8}$$

3. Stabilized finite element formulation

First of all, the governing equations in their primitive variables in Eq. (6) are spatially discretized into a semi-discrete form using the stabilized finite element formulation. Similar to the Navier–Stokes equation, the conservation of energy and species in Eqs. (6c) and (6d) include the advection terms, $(\boldsymbol{u}^* \cdot \nabla)\theta$ and $(\boldsymbol{u}^* \cdot \nabla)C$, too. The advection term causes the oscillatory velocity field in Galerkin projection method. Hence the residual-based stabilized finite element formulations, the Galerkin Least Squares (GLS) [31] and the Pressure Stabilizing Petrov–Galerkin (PSPG) [32], are employed to stabilize the spurious oscillation of the velocity field with numerical diffusion and circumvent the Ladyzhenskaya–Babuska–Brezzi (LBB) condition of the velocity–pressure field. To derive a finite element formulation, we define appropriate sets of finite trial solution spaces (S_u^h, S_t^h, S_c^h and S_p^h) for the velocity, the temperature, the species and the pressure, and their finite test function spaces (V_u^h, V_t^h, V_c^h and V_p^h) respectively in Eq. (9).

$$S_u^h = \{\boldsymbol{u}^{*h} | \boldsymbol{u}^{*h} \in (H^{1h})^d, \boldsymbol{u}^{*h} \doteq \tilde{\boldsymbol{u}}^{*h} \qquad \forall \boldsymbol{x}^* \in \Gamma_D^f(\tau)\} \tag{9a}$$

$$V_u^h = \{\boldsymbol{\psi}_u^h | \boldsymbol{\psi}_u^h \in (H^{1h})^d, \boldsymbol{\psi}_u^h \doteq \boldsymbol{0} \qquad \forall \boldsymbol{x}^* \in \Gamma_D^f(\tau)\} \tag{9b}$$

$$S_t^h = \{\theta^h | \theta^h \in H^{1h}, \theta^h \doteq \tilde{\theta}^h \qquad \forall \boldsymbol{x}^* \in \Gamma_D^f(\tau)\} \tag{9c}$$

$$V_t^h = \{\psi_t^h | \psi_t^h \in H^{1h}, \psi_t^h \doteq 0 \qquad \forall \boldsymbol{x}^* \in \Gamma_D^f(\tau)\} \tag{9d}$$

$$S_c^h = \{C^h | C^h \in H^{1h}, C^h \doteq \tilde{C}^h \qquad \forall \boldsymbol{x}^* \in \Gamma_D^f(\tau)\} \tag{9e}$$

$$V_c^h = \{\psi_c^h | \psi_c^h \in H^{1h}, \psi_c^h \doteq 0 \qquad \forall \boldsymbol{x}^* \in \Gamma_D^f(\tau)\} \tag{9f}$$

$$S_p^h = V_p^h = \{\psi_p^h | \psi_p^h \in H^{1h}\} \tag{9g}$$

where the superscript (h) indicates a finite function space, e.g., $S_u^h \subset S_u$. The value of d refers to the number of space dimension. H^{1h} is a finite dimensional space defined in Eq. (10), where P^1 is the piecewise linear polynomial and $\mathscr{E}$ denotes the set of elements resulting from the spatial discretization.

$$H^{1h} = \{\Theta^h | \Theta^h \in C^0, \Theta^h|_{\Omega^e} \in P^1, \forall \Omega^e \in \mathscr{E}\} \tag{10}$$

Hence the stabilized finite element formulation of Eq. (6) can be written as: for all $\boldsymbol{\psi}_u^h \in V_u^h$, $\psi_p^h \in V_p^h$, $\psi_t^h \in V_t^h$ and $\psi_c^h \in V_c^h$, find $\boldsymbol{u}^{*h} \in S_u^h$, $p^{*h} \in S_p^h$, $\theta^h \in S_t^h$ and $C^h \in S_c^h$ such that Eq. (11) is satisfied.

$$\mathscr{A}_P + \mathscr{A}_N + \mathscr{A}_G = 0 \tag{11}$$

where $\mathscr{A}_P$, $\mathscr{A}_N$ and $\mathscr{A}_G$ respectively refer to the terms associated with the Petrov–Galerkin method, the Nitsche's method and the Ghost penalty method in the proposed formulation. The detailed formulation of these terms will be discussed subsequently.

The stabilized finite element formulation for the Navier–Stokes equation and the conservation of energy and species ($\mathscr{A}_P$) is presented in Eq. (12),

$$\begin{aligned}
\mathscr{A}_P = & \underbrace{\int_{\Omega^f} \Big[\boldsymbol{\psi}_u^h \cdot \Big(\partial_\tau \boldsymbol{u}^{*h} + \big(\boldsymbol{u}_n^{*h} \cdot \nabla\big)\boldsymbol{u}^{*h} + \big(\boldsymbol{u}^{*h} \cdot \nabla\big)\boldsymbol{u}_n^{*h} - \big(\boldsymbol{u}_n^{*h} \cdot \nabla\big)\boldsymbol{u}_n^{*h} + (Ri\ \boldsymbol{n}_g)(\theta^h + Br\ C^h)\Big)\Big] d\Omega}_{\mathscr{B}_G([\boldsymbol{\psi}_u^h, \psi_p^h], [\boldsymbol{u}^{*h}, p^{*h}, \theta^h, C^h])} \\
& \underbrace{+ \int_{\Omega^f} \Big[\epsilon(\boldsymbol{\psi}_u^h) : \boldsymbol{\sigma}\{\boldsymbol{u}^{*h}, p^{*h}\}\Big] d\Omega - \int_{\Gamma_N^f} \boldsymbol{\psi}_u^h \cdot \tilde{\boldsymbol{h}}^{*h}\, d\Gamma + \int_{\Omega^f} \big[\psi_p^h \nabla \cdot \boldsymbol{u}^{*h}\big] d\Omega}_{\mathscr{B}_G([\boldsymbol{\psi}_u^h, \psi_p^h], [\boldsymbol{u}^{*h}, p^{*h}, \theta^h, C^h])} \\
& \underbrace{- \int_{\Gamma_{N(out)}^f} \boldsymbol{\psi}_u^h \cdot \big[-\frac{1}{Re}(\nabla \boldsymbol{u}^{*h})' \cdot \boldsymbol{n}\big] d\Gamma}_{\mathscr{B}_{corr}(\boldsymbol{\psi}_u^h, \boldsymbol{u}^{*h})} + \underbrace{\sum_{e=1}^{n_{el}} \int_{\Omega^f} \tau_u \Big[\big(\boldsymbol{u}_n^{*h} \cdot \nabla\big)\boldsymbol{\psi}_u^h - \frac{1}{Re}\nabla^2 \boldsymbol{\psi}_u^h + \nabla \psi_p^h\Big] \cdot}_{\mathscr{B}_S([\boldsymbol{\psi}_u^h, \psi_p^h], [\boldsymbol{u}^{*h}, p^{*h}, \theta^h, C^h])} \\
& \underbrace{\Big[\partial_\tau \boldsymbol{u}^{*h} + \big(\boldsymbol{u}_n^{*h} \cdot \nabla\big)\boldsymbol{u}^{*h} - \frac{1}{Re}\nabla^2 \boldsymbol{u}^{*h} + \nabla p^{*h} + (Ri\ \boldsymbol{n}_g)(\theta^h + Br\ C^h)\Big] d\Omega}_{\mathscr{B}_S([\boldsymbol{\psi}_u^h, \psi_p^h], [\boldsymbol{u}^{*h}, p^{*h}, \theta^h, C^h])} \\
& \underbrace{+ \sum_{e=1}^{n_{el}} \int_{\Omega^f} \tau_p \Big[(\nabla \cdot \boldsymbol{\psi}_u^h)(\nabla \cdot \boldsymbol{u}^{*h})\Big] d\Omega}_{\mathscr{B}_S([\boldsymbol{\psi}_u^h, \psi_p^h], [\boldsymbol{u}^{*h}, p^{*h}, \theta^h, C^h])} \\
& \underbrace{+ \int_{\Omega^f} \Big[\psi_t^h \cdot \big(\partial_\tau \theta^h + \big(\boldsymbol{u}_n^{*h} \cdot \nabla\big)\theta^h + \big(\boldsymbol{u}^{*h} \cdot \nabla\big)\theta_n^h - \big(\boldsymbol{u}_n^{*h} \cdot \nabla\big)\theta_n^h\big) + \frac{1}{Re\ Pr}\nabla \psi_t^h \cdot \nabla \theta^h\Big] d\Omega}_{\mathscr{B}_G(\psi_t^h, [\boldsymbol{u}^{*h}, \theta^h])} \\
& \underbrace{+ \sum_{e=1}^{n_{el}} \int_{\Omega^f} \tau_t \Big[\big(\boldsymbol{u}_n^{*h} \cdot \nabla\big)\psi_t^h - \frac{1}{Re\ Pr}\nabla^2 \psi_t^h\Big] \cdot \Big[\partial_\tau \theta^h + \big(\boldsymbol{u}_n^{*h} \cdot \nabla\big)\theta^h - \frac{1}{Re\ Pr}\nabla^2 \theta^h\Big] d\Omega}_{\mathscr{B}_S(\psi_t^h, [\boldsymbol{u}^{*h}, \theta^h])} \underbrace{- \int_{\Gamma_N^f} \big[\psi_t^h \tilde{q}^{*h}\big] d\Gamma}_{\mathscr{B}_G(\psi_t^h, \theta^h)} \\
& \underbrace{+ \int_{\Omega^f} \Big[\psi_c^h \cdot \big(\partial_\tau C^h + \big(\boldsymbol{u}_n^{*h} \cdot \nabla\big)C^h + \big(\boldsymbol{u}^{*h} \cdot \nabla\big)C_n^h - \big(\boldsymbol{u}_n^{*h} \cdot \nabla\big)C_n^h\big) + \frac{1}{Le\ Re\ Pr}\nabla \psi_c^h \cdot \nabla C^h\Big] d\Omega}_{\mathscr{B}_G(\psi_c^h, [\boldsymbol{u}^{*h}, C^h])}
\end{aligned}$$

$$+\underbrace{\sum_{e=1}^{n_{el}}\int_{\Omega^f}\tau_c\Big[\big(\boldsymbol{u}_n^{*h}\cdot\nabla\big)\psi_c^h-\frac{1}{Le\ Re\ Pr}\nabla^2\psi_c^h\Big]\cdot}_{\mathscr{B}_S(\psi_c^h,[\boldsymbol{u}^{*h},C^h])}$$

$$\underbrace{\Big[\partial_\tau C^h+\big(\boldsymbol{u}_n^{*h}\cdot\nabla\big)C^h-\frac{1}{Le\ Re\ Pr}\nabla^2C^h\Big]d\Omega}_{\mathscr{B}_S(\psi_c^h,[\boldsymbol{u}^{*h},C^h])}-\underbrace{\int_{\Gamma_N^f}\big[\psi_c^h\tilde{f}^{*h}\big]d\Gamma}_{\mathscr{B}_G(\psi_c^h,C^h)} \tag{12}$$

where the terms of $\mathscr{B}_G(\cdot)$ are derived from the standard continuous Galerkin method for the unsteady incompressible Navier–Stokes equation and the conservation of energy and species. In Eq. (12), the nonlinear incompressible Navier–Stokes equation and the conservation of energy and species are linearized by Newton linearization to achieve the quadratic convergence, and the solution at each time step is updated in iterations until convergence. The variable $\boldsymbol{u}_n^{*h}$, θ_n^h and C_n^h are the velocity, the temperature and the species concentration in the last iteration step. Upon convergence, the terms $\big(\boldsymbol{u}_n^{*h}\cdot\nabla\big)\boldsymbol{u}^{*h}+\big(\boldsymbol{u}^{*h}\cdot\nabla\big)\boldsymbol{u}_n^{*h}-\big(\boldsymbol{u}_n^{*h}\cdot\nabla\big)\boldsymbol{u}_n^{*h}$, $\big(\boldsymbol{u}_n^{*h}\cdot\nabla\big)\theta^h+\big(\boldsymbol{u}^{*h}\cdot\nabla\big)\theta_n^h-\big(\boldsymbol{u}_n^{*h}\cdot\nabla\big)\theta_n^h$ and $\big(\boldsymbol{u}_n^{*h}\cdot\nabla\big)C^h+\big(\boldsymbol{u}^{*h}\cdot\nabla\big)C_n^h-\big(\boldsymbol{u}_n^{*h}\cdot\nabla\big)C_n^h$ reduce to $\big(\boldsymbol{u}^{*h}\cdot\nabla\big)\boldsymbol{u}^{*h}$, $\big(\boldsymbol{u}^{*h}\cdot\nabla\big)\theta^h$ and $\big(\boldsymbol{u}^{*h}\cdot\nabla\big)C^h$ respectively. The boundary integral $\mathscr{B}_{corr}(\boldsymbol{\psi}_u^h,\boldsymbol{u}^{*h})$ is a correction term for the "do-nothing" outflow boundary condition to avoid reverse numerical flux [33]. The terms of $\mathscr{B}_S(\cdot)$ in Eq. (12) are the stabilization terms based on GLS and PSPG formulations. The stabilization parameters (τ_u, τ_p, τ_t and τ_c) are defined as

$$\tau_u=\Big[\Big(\frac{2}{dt}\Big)^2+\Big(\frac{2\|\boldsymbol{u}^*\|}{l_e}\Big)^2+9\Big(\frac{4}{Re\ {l_e}^2}\Big)^2\Big]^{-1/2} \tag{13a}$$

$$\tau_p=\frac{l_e}{2}\|\boldsymbol{u}^*\|\gamma\quad\text{for }\gamma=\begin{cases}Re_u/3 & 0\leqslant Re_u\leqslant 3\\ 1 & 3<Re_u\end{cases} \tag{13b}$$

$$\tau_t=\Big[\Big(\frac{2}{dt}\Big)^2+\Big(\frac{2\|\boldsymbol{u}^*\|}{l_e}\Big)^2+9\Big(\frac{4}{Re\ Pr\ {l_e}^2}\Big)^2\Big]^{-1/2} \tag{13c}$$

$$\tau_c=\Big[\Big(\frac{2}{dt}\Big)^2+\Big(\frac{2\|\boldsymbol{u}^*\|}{l_e}\Big)^2+9\Big(\frac{4}{Le\ Re\ Pr\ {l_e}^2}\Big)^2\Big]^{-1/2} \tag{13d}$$

where Re_u and l_e respectively are defined as cell Reynolds number and the characteristic element length. It is noteworthy that the GLS and PSPG stabilizations are used for finite elements within flow domain, except the cut cells (the element cut by the embedded interface). For cut cells, the Ghost penalty method replaces the GLS and PSPG stabilizations instead. The details will be furnished in Section 3.2.

3.1. Nitsche's method for heat and mass transfer

The symmetric and non-symmetric Nitsche's methods ($\mathscr{A}_N$) are shown in Eq. (14),

$$\mathscr{A}_N=\underbrace{\gamma_{u1}\int_{\Gamma^{fs}}\boldsymbol{\psi}_u^h(\boldsymbol{u}^{*h}-\tilde{\boldsymbol{u}}^{*h})d\Gamma-\int_{\Gamma^{fs}}\boldsymbol{\psi}_u^h(\boldsymbol{\sigma}\{\boldsymbol{u}^{*h},p^{*h}\}\cdot\boldsymbol{n})d\Gamma}_{\mathscr{B}_N([\boldsymbol{\psi}_u^h,\psi_p^h],[\boldsymbol{u}^{*h},p^{*h}])}$$

$$\underbrace{-\gamma_{u2}\int_{\Gamma^{fs}}(\boldsymbol{\sigma}\{\boldsymbol{\psi}_u^h,\psi_p^h\}\cdot\boldsymbol{n})(\boldsymbol{u}^{*h}-\tilde{\boldsymbol{u}}^{*h})d\Gamma}_{\mathscr{B}_N([\boldsymbol{\psi}_u^h,\psi_p^h],[\boldsymbol{u}^{*h},p^{*h}])}$$

$$\underbrace{-\int_{\Gamma^{fs-}}\boldsymbol{\psi}_u^h\big((\boldsymbol{u}^{*h}-\tilde{\boldsymbol{u}}^{*h})\cdot\boldsymbol{n}\big)(\boldsymbol{u}^{*h}-\tilde{\boldsymbol{u}}^{*h})d\Gamma}_{\mathscr{B}_N([\boldsymbol{\psi}_u^h,\psi_p^h],[\boldsymbol{u}^{*h},p^{*h}])}$$

$$\underbrace{+\gamma_{t1}\int_{\Gamma^{fs}}\psi_t^h(\theta^h-\tilde{\theta}^h)d\Gamma-\int_{\Gamma^{fs}}\psi_t^h\Big(\frac{1}{Re\ Pr}\nabla\theta^h\cdot\boldsymbol{n}\Big)d\Gamma}_{\mathscr{B}_N(\psi_t^h,\theta^h)}$$

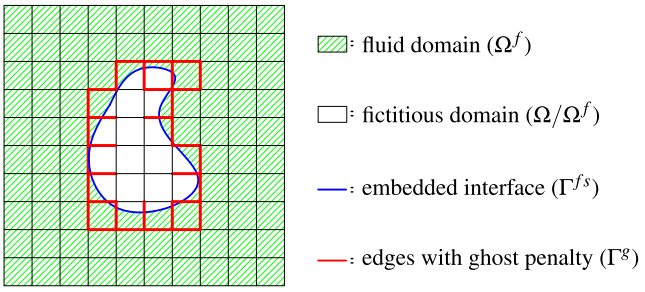

Fig. 1. Schematic diagram of an embedded interface with Ghost penalty terms.

$$
\begin{aligned}
&\underbrace{-\gamma_{t2}\int_{\Gamma^{fs}}\left(\frac{1}{Re\ Pr}\nabla\psi_t^h\cdot\boldsymbol{n}\right)(\theta^h-\tilde{\theta}^h)d\Gamma}_{\mathscr{B}_N(\psi_t^h,\theta^h)}\\
&\underbrace{+\gamma_{c1}\int_{\Gamma^{fs}}\psi_c^h(C^h-\tilde{C}^h)d\Gamma-\int_{\Gamma^{fs}}\psi_c^h\left(\frac{1}{Le\ Re\ Pr}\nabla C^h\cdot\boldsymbol{n}\right)d\Gamma}_{\mathscr{B}_N(\psi_c^h,C^h)}\\
&\underbrace{-\gamma_{c2}\int_{\Gamma^{fs}}\left(\frac{1}{Le\ Re\ Pr}\nabla\psi_c^h\cdot\boldsymbol{n}\right)(C^h-\tilde{C}^h)d\Gamma}_{\mathscr{B}_N(\psi_c^h,C^h)}
\end{aligned}
\tag{14}
$$

where $\mathscr{B}_N([\boldsymbol{\psi}_u^h,\psi_p^h],[\boldsymbol{u}^{*h},p^{*h}])$, $\mathscr{B}_N(\psi_t^h,\theta^h)$ and $\mathscr{B}_N(\psi_c^h,C^h)$ are the terms of the Nitsche's method for the flow, the temperature and the species concentration fields respectively. $\boldsymbol{n}$ is the outward normal vector along the embedded interface (pointing into the fictitious domain). γ_u, γ_t and γ_c respectively are the penalty terms for the velocity, the temperature and the species concentration. The $\gamma_{u2}=\gamma_{t2}=\gamma_{c2}=1$ corresponds to the symmetric Nitsche's method; whereas $\gamma_{u2}=\gamma_{t2}=\gamma_{c2}=-1$ is used in the non-symmetric Nitsche's method. $\gamma_{u1}\in\frac{1}{Re\ l_e}[10^2,10^3]$, $\gamma_{t1}\in\frac{1}{Re\ Pr\ l_e}[10^2,10^3]$ and $\gamma_{c1}\in\frac{1}{Le\ Re\ Pr\ l_e}[10^2,10^3]$ are chosen to stabilized Nitsche's methods. Both symmetric and non-symmetric Nitsche's methods can be employed in the proposed numerical formulation. The non-symmetric variance differentiates from the symmetric variance in term of the characteristics of convergence. For the symmetric variance, the penalty parameters (γ_{u1}, γ_{t1} and γ_{c1}) are required to be large enough to ensure the convergence of solution. In contrast, the restriction for these penalty parameters is less stringent in the non-symmetric Nitsche's method. The non-symmetric Nitsche's method is also stable without these penalty parameters [18]. However, the convergence of penalty-free non-symmetric Nitsche's method is not guaranteed while the 1-order polynomial is used [34]. In addition, the non-symmetric Nitsche's method is also known for its sub-optimal convergence and lack of adjoint consistency [19]. To improve the robustness of the proposed numerical formulation, the penalty parameters (γ_{u1}, γ_{t1} and γ_{c1}) are chosen large enough for both symmetric and non-symmetric Nitsche's methods in order to guarantee the convergence of the solution. Upon the convergence of solution ($\boldsymbol{u}^{*h}\approx\tilde{\boldsymbol{u}}^{*h}$, $\theta^{*h}\approx\tilde{\theta}^{*h}$ and $C^{*h}\approx\tilde{C}^{*h}$), all penalty terms in both symmetric and non-symmetric Nitsche's methods in Eq. (14) vanish. The line integral along Γ^{fs-} is an upwind term [20] to enhance the robustness of numerical formulation for fast-moving immersed interfaces through background meshes. The Γ^{fs-} boundary is defined as the "inflow" part of Γ^{fs} as

$$
\Gamma^{fs-}=\{\boldsymbol{x}\mid(\boldsymbol{u}^{*h}-\tilde{\boldsymbol{u}}^{*h})\cdot\boldsymbol{n}<0.0,\quad\forall\boldsymbol{x}\Gamma^{fs}\}
\tag{15}
$$

3.2. Cut cell stabilization and fictitious domain

A cut cell is an element that is demarcated by an embedded interface, e.g., the blue circle in Fig. 1, into the active fluid domain and the fictitious domain respectively. In this study, the embedded interface is represented by a level-set function. If the solution to the level-set function is larger than zero, it indicates the fluid domain (Ω^f) and vice versa for the fictitious domain (Ω/Ω^f). If the physical part is very small, some basis functions have little

support inside the physical domain. It leads to the large condition numbers of system matrix. To alleviate the jumps of solutions across an embedded interface, the Ghost penalty method [17] is implemented along the edges of cut cells, the red edges in Fig. 1. The specific terms of the Ghost penalty are listed in Eq. (16).

$$\begin{aligned}\mathscr{A}_G &= \beta_u^{gp}\frac{1}{Re}G(\boldsymbol{\psi}_u^h,\boldsymbol{u}^{*h}) + \beta_p^{gp}Re\ g(\psi_p^h,p^{*h}) \\ &\quad + \beta_t^{gp}\frac{1}{Re\ Pr}G(\psi_t^h,\theta^h) + \beta_c^{gp}\frac{1}{Le\ Re\ Pr}G(\psi_c^h,C^h) \qquad (16)\\ g(\psi_p^h,p^{*h}) &= \sum_{k=1}^{e} l_k^3\int_{\Gamma g}[[\frac{\partial^\alpha\psi_p^h}{\partial\boldsymbol{n}^\alpha}]][[\frac{\partial^\alpha p^{*h}}{\partial\boldsymbol{n}^\alpha}]]dl_k \\ G(\boldsymbol{\psi}_u^h,\boldsymbol{u}^{*h}) &= \sum_{k=1}^{e}\sum_{i=1}^{d} l_k\int_{\Gamma g}[[\frac{\partial^\alpha\psi_{u(i)}^h}{\partial\boldsymbol{n}^\alpha}]][[\frac{\partial^\alpha u_{(i)}^{*h}}{\partial\boldsymbol{n}^\alpha}]]dl_k \\ G(\psi_t^h,\theta^h) &= \sum_{k=1}^{e} l_k\int_{\Gamma g}[[\frac{\partial^\alpha\psi_t^h}{\partial\boldsymbol{n}^\alpha}]][[\frac{\partial^\alpha\theta^h}{\partial\boldsymbol{n}^\alpha}]]dl_k \\ G(\psi_c^h,C^h) &= \sum_{k=1}^{e} l_k\int_{\Gamma g}[[\frac{\partial^\alpha\psi_c^h}{\partial\boldsymbol{n}^\alpha}]][[\frac{\partial^\alpha C^h}{\partial\boldsymbol{n}^\alpha}]]dl_k\end{aligned}$$

where Γ^g refers to the edges of cut cell where the Ghost penalty term is imposed. The first two terms in Eq. (16) are used to alleviate the jumps of velocity gradients and pressure values over the embedded interface. The third and fourth terms are utilized to stabilize the jumps of temperature and species. e and d respectively refer to the number of edges of cut cell imposed with Ghost penalty terms and the dimension of problem. α and l are the order of derivative and the length of element's edge respectively. The operator $[[\cdot]]$ denotes a jump of solution across the element edge, which is defined as

$$[[\Lambda]] = \Lambda^-\boldsymbol{n}^- + \Lambda^+\boldsymbol{n}^+; \quad [[\boldsymbol{\Lambda}]] = \boldsymbol{\Lambda}^-\cdot\boldsymbol{n}^- + \boldsymbol{\Lambda}^+\cdot\boldsymbol{n}^+ \qquad (17a)$$

$$[[\frac{\partial\Lambda}{\partial\boldsymbol{n}}]] = \left(\frac{\partial\Lambda}{\partial\boldsymbol{x}}\right)^-\cdot\boldsymbol{n}^- + \left(\frac{\partial\Lambda}{\partial\boldsymbol{x}}\right)^+\cdot\boldsymbol{n}^+ \qquad (17b)$$

where Λ and $\boldsymbol{\Lambda}$ are arbitrary scalar and vector quantities respectively. $\boldsymbol{n}$ is the outward normal vector of an element's edge. The superscripts (+ and -) refer to the left and right-hand sides of the element's edge.

A detailed study of the performance of the Ghost penalty method for the incompressible Navier–Stokes equation was reported by Dettmer et al. (2016) [26]. In this study, the performance of the Ghost penalty algorithm for heat & mass transfer is assessed in a canonical benchmark case, the double-diffusive mixed convection in an enclosure with an embedded cylinder, as shown in Fig. 2(a). The values of the dimensionless groups are chosen as $Re = 20$, $Pr = 0.7$, $Ri = 0.1$, $Br = 1.0$ and $Le = 5.0$. The size of computational domain is $2L \times 2L$, where $L = 1.0$ is the diameter of the embedded cylinder (the blue dotted line) in the center. The sizes of inlet and outlet are both $0.2L$. The assessments are conducted in two mesh resolutions, 20×20 and 40×40. Γ_e, Γ_w, Γ_n and Γ_s respectively are the East, West, North and South boundaries. The inlet Γ_{inlet} is located in the left-down corner of the domain with an inflow velocity $\boldsymbol{u}^* = [U_\infty, 0]'$. On the other hand, the outlet Γ_{outlet} is situated in the top-right corner of the domain. The following boundary conditions are imposed along the boundaries of the computational domain in Fig. 2(a).

- $u^* = U_\infty = 1.0;\ v^* = \theta = C = 0.0; \quad \forall\boldsymbol{x} \in \Gamma_{inlet}$
- $p^* = 0.0 \quad \forall\boldsymbol{x} \in \Gamma_{outlet}$
- $\boldsymbol{u}^* = 0.0;\ \frac{\partial\theta}{\partial\boldsymbol{n}} = \frac{\partial C}{\partial\boldsymbol{n}} = 0.0 \quad \forall\boldsymbol{x} \in \Gamma_w \cup \Gamma_e \cup \Gamma_n \cup \Gamma_s$
- $\boldsymbol{u}^* = 0.0;\ T = C = 1.0 \quad \forall\boldsymbol{x} \in \Gamma_{cyl}$

The penalty parameters of Nitsche's method are chosen as $\gamma_{u1} = 500/(Re\ l_e)$, $\gamma_{t1} = 500/(Re\ Pr\ l_e)$ and $\gamma_{c1} = 500/(Le\ Re\ Pr\ l_e)$ respectively. To evaluate the performance of the Ghost penalty method for heat & mass transfer, the corresponding penalty parameters are chosen as $\beta^{gp} = \beta_u^{gp} = \beta_p^{gp} = \beta_t^{gp} = \beta_c^{gp} \in 1 \times [10^{-11}, 10^{10}]$. The condition number and $\mathscr{L}_2$ norm of the system matrix are employed as the metrics to evaluate its performance in Fig. 2(b). It shows that the condition numbers are minimized within the range of $\beta^{gp} \in [10^{-4}, 10]$. The condition

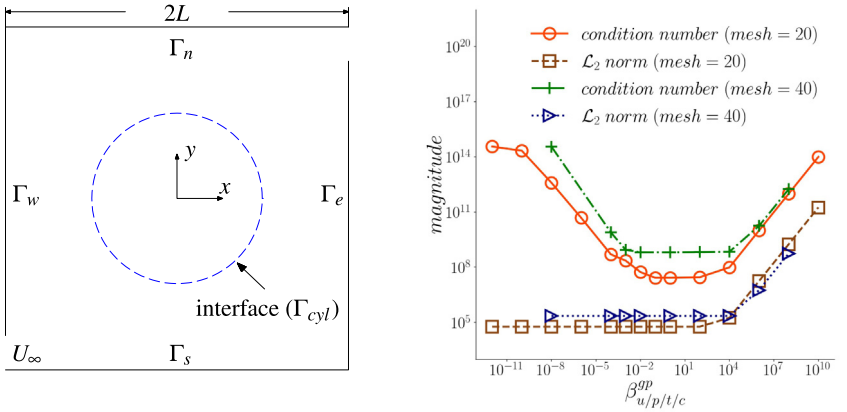

(a) (b)

Fig. 2. Performance of Ghost penalty stabilization: (a) schematic diagram of double-diffusive mixed convection in an enclosure with an embedded cylinder; (b) change of the condition number and $\mathscr{L}_2$ norm of system matrix with respect to the penalty parameters. $mesh = 20$ and $mesh = 40$ refer to the mesh resolution 20×20 and 40×40 respectively.

number and $\mathscr{L}_2$ norm of the original system matrix without the Ghost penalty terms ($\beta^{gp} \lesssim 1 \times 10^{-11}$) respectively are within the order of magnitudes 10^{15} and 10^{5}. On the other hands as $\beta^{gp} \gtrsim 10$, the Ghost penalty terms cause a significant spike of $\mathscr{L}_2$ norm. Therefore, the penalty parameters are chosen as $\beta^{gp} = 0.01$ [26] for the numerical examples in this study.

To further improve the overall stability of the system matrix, an iterative solver, e.g., Generalized Minimal Residual Method (GMRES), together with Additive Schwarz Method (ASM) preconditioning can be employed for finite cell formulations [35]. In the fictitious domain, including the triangulated parts of cut cells inside fictitious domain, the numerical integration of the finite element formulation ($\mathscr{A}_P$) in Eq. (12) is not computed such that the solutions inside the fictitious domain have no influence to the solutions inside the active (physical) flow field. A sub-matrix is extracted from the system matrix, so the elements inside the fictitious domain are eliminated from computation.

3.3. Projection-based adaptive Gauss quadrature (PAGQ)

In the proposed formulation, the projection-based adaptive Gauss quadrature(PAGQ) scheme [24] is employed for the numerical integration inside the cut cells with embedded discontinuities. In PAGQ, the cut cell is sub-divided into smaller integration cells along the embedded interface, the blue lines in Fig. 3. The yellow dots are the Gauss integration points. The red lines are the elemental edges imposed with the Ghost penalty terms. A number of construction lines, the green lines in Fig. 3, are introduced to facilitate the triangulation such that the embedded interface aligns with the edges of integration cells. In each integration cell, the standard Gauss quadrature rule is used for the numerical integration without worrying discontinuity, since the embedded interface is aligned with its edges. In this way, the embedded interface is treated as a boundary integral in standard continuous finite element method.

For each integration cell, it results in a set of elemental matrices of its own, e.g., $\boldsymbol{M}_s$, $\boldsymbol{K}_s$ and $\boldsymbol{F}_s$. For example, the elemental characteristic matrix ($\boldsymbol{K}_s$) of the integration cell is projected by a transformation tensor ($\mathscr{T}$) into the solution space of its parent cut cell, which leads to a reconstructed matrix $\boldsymbol{K}^r_s$. Subsequently, the projected elemental matrices of integration cells are summed up to form the reconstructed elemental matrices of their parent cut cell, e.g., $\boldsymbol{M}^r_c$, $\boldsymbol{K}^r_c$ and $\boldsymbol{F}^r_c$ in Eq. (18). These reconstructed elemental matrices assembled by an adaptive Gauss quadrature rules are equivalent to the elemental matrices obtained by the standard Gauss quadrature rules over the parent cut cell [24]. The assembly procedures and the construction of transformation tensor are presented in Eq. (18),

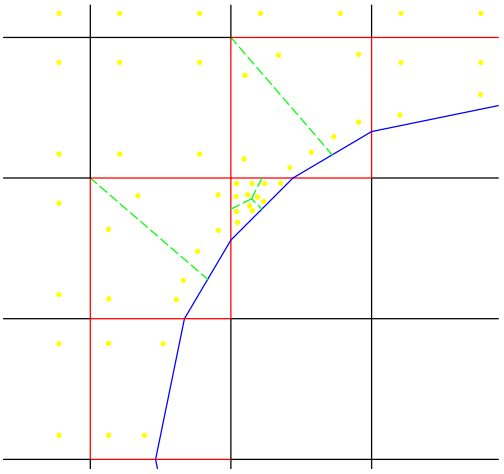

Fig. 3. Schematic diagram of PAGQ numerical integration scheme for bilinear quadrilateral elements.

where $\boldsymbol{N}_c$ is the shape functions of the parent cut cell. $\{\boldsymbol{n}\}$ and $\{\boldsymbol{s}\}$ respectively are the sets of nodes of the parent cut cell (physical nodes) and its sub-divided integration cells (dummy nodes). For the detailed discussion of the PAGQ scheme and the analyzes of numerical formulation based on the Nitsche's methods, please refer to Liu & Tan (2020) [24].

$$\boldsymbol{M}_c \equiv \boldsymbol{M}_c^r = \sum_i^n \mathscr{T}' \boldsymbol{M}_s \mathscr{T} \tag{18a}$$

$$\boldsymbol{K}_c \equiv \boldsymbol{K}_c^r = \sum_i^n \mathscr{T}' \boldsymbol{K}_s \mathscr{T} \tag{18b}$$

$$\boldsymbol{F}_c \equiv \boldsymbol{F}_c^r = \sum_i^n \mathscr{T}' \boldsymbol{F}_s \tag{18c}$$

$$\mathscr{T} = \begin{bmatrix} N_{c(n_1)}(s_1) & N_{c(n_2)}(s_1) & \dots & N_{c(n_j)}(s_1) \\ N_{c(n_1)}(s_2) & N_{c(n_2)}(s_2) & \dots & N_{c(n_j)}(s_2) \\ \vdots & \vdots & \ddots & \vdots \\ N_{c(n_1)}(s_i) & N_{c(n_2)}(s_i) & \dots & N_{c(n_j)}(s_i) \end{bmatrix} \tag{18d}$$

3.4. Interface conditions

The fluid solver is coupled with the structural solver by satisfying the kinematic and the dynamic constraints along the fluid–structure interface (Γ^{fs}), as shown in Eq. (19).

$$\boldsymbol{u}^*(\boldsymbol{\Phi}^*(\mathscr{X},\tau),\tau) = \partial_\tau \boldsymbol{\Phi}^*(\mathscr{X},\tau) \qquad \forall \mathscr{X} \in \Gamma^{fs}(\tau) \tag{19a}$$

$$\boldsymbol{h}^*(\boldsymbol{\Phi}^*(\mathscr{X},\tau),\tau) = -\boldsymbol{h}^{*cyl}(\boldsymbol{\Phi}^*(\mathscr{X},\tau),\tau) \qquad \forall \mathscr{X} \in \Gamma^{fs}(\tau) \tag{19b}$$

where $\boldsymbol{h}^*$ and $\boldsymbol{h}^{*cyl} = [h_x^{*cyl}, h_y^{*cyl}]$ respectively are the dimensionless fluid and structural stresses along the fluid–structure interface. The value of $\boldsymbol{\Phi}^*$ is the dimensionless location of the structure, which is defined in Eq. (20), where $\boldsymbol{\eta}^*$ is the dimensionless displacement of structure at time τ. The values of $\partial_\tau \boldsymbol{\Phi}^*$ and $\partial_\tau^2 \boldsymbol{\Phi}^*$ are defined as the structural velocity and acceleration respectively.

$$\boldsymbol{\Phi}^*(\mathscr{X},\tau) = \boldsymbol{\eta}^*(\mathscr{X},\tau) + \mathscr{X} \quad \forall \mathscr{X} \in \Omega^s(\tau) \tag{20}$$

The superscript (s) indicates the structural variables. Hence the governing equation of the structure can be formulated as follows

$$\begin{aligned}
&\partial_\tau^2 \boldsymbol{\Phi}^* + \boldsymbol{c}^s \partial_\tau \boldsymbol{\Phi}^* + \boldsymbol{k}^s \boldsymbol{\eta}^* = \boldsymbol{h}^{*cyl} \quad \forall \mathscr{X} \in \Omega^s(\tau) \\
&\boldsymbol{c}^s = 2\zeta \sqrt{\boldsymbol{k}^s m^s}; \quad \boldsymbol{k}^s = (2\pi \boldsymbol{f}_n)^2 m^s \\
&Ur = U_\infty/(f_{ny} D); \quad m^s = m^*(0.25\pi L^2 \rho_0)
\end{aligned} \tag{21}$$

where $\boldsymbol{c}^s = [c_x^s, c_y^s]'$, $\boldsymbol{k}^s = [k_x^s, k_y^s]'$ and $\boldsymbol{f}_n = [f_{nx}, f_{ny}]'$ respectively are the resultant damping coefficient vector, the resultant stiffness coefficient vector and the structural frequency vector. m^* is the mass ratio and ζ is the damping ratio. The reduced velocity (Ur) is defined based on the structural frequency in the transverse direction (f_{ny}). In this investigation, it is assumed that the structural frequencies in transverse and streamwise directions are identical. The values of $L = 1.0$ and m^s are the diameter and mass of the cylinder.

3.5. Time integration and fluid–structure coupling scheme

The second-order accurate and unconditionally stable generalized-α scheme is employed for both the heat & mass transfer and the structure equations in the proposed numerical formulation. The generalized-α scheme belongs to the α-family time integration schemes, in which the numerical solution is solved at fractional time steps and subsequently projected forward in time.

For the heat & mass transfer equations, the system of equation can be represented as the form in Eq. (22) and their solutions at the fractional steps [36] are defined in Eq. (23) below,where ρ_∞ is the spectral radius controlling the damping in frequency domain. The definitions in Eq. (23e) guarantee that the time integration is unconditionally stable and second order accurate [36]. Assuming that the resultant linear system of the stabilized finite element formulation for heat & mass transfer at two consecutive time steps can be written into the matrix form in Eq. (24).

$$\boldsymbol{M} \cdot \partial_\tau \boldsymbol{u}^{*h} + \boldsymbol{K} \cdot \boldsymbol{u}^{*h} = \boldsymbol{F} \tag{22}$$

$$\partial_\tau \boldsymbol{u}^{*h}_{\tau+\alpha_m^f} = (1-\alpha_m^f)\, \partial_\tau \boldsymbol{u}^{*h}_\tau + \alpha_m^f\, \partial_\tau \boldsymbol{u}^{*h}_{\tau+1} \tag{23a}$$

$$\boldsymbol{u}_{\tau+\alpha_f^f} = (1-\alpha_f^f)\, \boldsymbol{u}^{*h}_\tau + \alpha_f^f\, \boldsymbol{u}^{*h}_{\tau+1} \tag{23b}$$

$$\boldsymbol{F}_{n+\alpha_f^f} = (1-\alpha_f^f)\, \boldsymbol{F}_\tau + \alpha_f^f\, \boldsymbol{F}_{\tau+1} \tag{23c}$$

$$\frac{\boldsymbol{u}^{*h}_{\tau+1} - \boldsymbol{u}^{*h}_\tau}{d\tau} = (1-\gamma^f)\partial_\tau \boldsymbol{u}^{*h}_\tau + \gamma^f \partial_\tau \boldsymbol{u}^{*h}_{\tau+1} \tag{23d}$$

$$\alpha_m^f = \frac{1}{2}\frac{3-\rho_\infty}{1+\rho_\infty};\ \alpha_f^f = \frac{1}{1+\rho_\infty};\ \gamma^f = \frac{1}{2} + \alpha_m^f - \alpha_f^f \tag{23e}$$

$$\boldsymbol{M} \cdot \partial_\tau \boldsymbol{u}^{*h}_\tau + \boldsymbol{K}_\tau \cdot \boldsymbol{u}^{*h}_\tau = \boldsymbol{F}_\tau \tag{24a}$$

$$\boldsymbol{M} \cdot \partial_\tau \boldsymbol{u}^{*h}_{\tau+1} + \boldsymbol{K}_{\tau+1} \cdot \boldsymbol{u}^{*h}_{\tau+1} = \boldsymbol{F}_{\tau+1} \tag{24b}$$

where it is assumed that the mass matrix $(\boldsymbol{M})$ is independent of time; whereas the characteristic matrix $(\boldsymbol{K})$ and the force vector $(\boldsymbol{F})$ will change at the different time steps. Substituting Eq. (24) into Eq. (23d), the solution at the next time step $(\boldsymbol{u}_{\tau+1})$ can be computed by the expression in Eq. (25), where $d\tau$ is the time step size.

$$\begin{aligned}
&\hat{\boldsymbol{K}}_{\tau+1} \cdot \boldsymbol{u}^{*h}_{\tau+1} = \hat{\boldsymbol{K}}_\tau \cdot \boldsymbol{u}^{*h}_\tau + \hat{\boldsymbol{F}}_{\tau,\tau+1} \\
&\hat{\boldsymbol{K}}_{\tau+1} = \boldsymbol{M} + \gamma^f\, d\tau\, \boldsymbol{K}_{\tau+1}; \quad \hat{\boldsymbol{K}}_\tau = \boldsymbol{M} - (1-\gamma^f)\, d\tau\, \boldsymbol{K}_\tau \\
&\hat{\boldsymbol{F}}_{\tau,\tau+1} = d\tau\, [\gamma^f\, \boldsymbol{F}_{\tau+1} + (1-\gamma^f)\, \boldsymbol{F}_\tau]
\end{aligned} \tag{25}$$

The similar derivation procedures of the generalized-α time integration scheme can be applied to the structure equation too. Based on Eq. (21), the system of equation representing the structural dynamics can be written in the form in Eq. (26), where the mass $(\boldsymbol{M})$, the damping $(\boldsymbol{C})$ and the stiffness $(\boldsymbol{K})$ matrices are assumed to be independent on time.

$$\boldsymbol{M} \cdot \partial_\tau^2 \boldsymbol{\eta}^* + \boldsymbol{C} \cdot \partial_\tau \boldsymbol{\eta}^* + \boldsymbol{K} \cdot \boldsymbol{\eta}^* = \boldsymbol{F} \tag{26}$$

The solutions to the structure equation at the fractional steps [37] can be defined as

$$\partial_\tau^2 \boldsymbol{\eta}^*_{\tau+1-\alpha_m^s} = (1-\alpha_m^s)\ \partial_\tau^2 \boldsymbol{\eta}^*_{\tau+1} + \alpha_m^s\ \partial_\tau^2 \boldsymbol{\eta}^*_{\tau} \tag{27a}$$

$$\partial_\tau \boldsymbol{\eta}^*_{\tau+1-\alpha_f^s} = (1-\alpha_f^s)\ \partial_\tau \boldsymbol{\eta}^*_{\tau+1} + \alpha_f^s\ \partial_\tau \boldsymbol{\eta}^*_{\tau} \tag{27b}$$

$$\boldsymbol{\eta}^*_{\tau+1-\alpha_f^s} = (1-\alpha_f^s)\ \boldsymbol{\eta}^*_{\tau+1} + \alpha_f^s\ \boldsymbol{\eta}^*_{\tau} \tag{27c}$$

$$\boldsymbol{F}_{n+1-\alpha_f^s} = (1-\alpha_f^s)\ \boldsymbol{F}_{\tau+1} + \alpha_f^s\ \boldsymbol{F}_{\tau} \tag{27d}$$

$$\frac{\partial_\tau \boldsymbol{\eta}^*_{\tau+1} - \partial_\tau \boldsymbol{\eta}^*_{\tau}}{d\tau} = (1-\gamma^s)\partial_\tau^2 \boldsymbol{\eta}^*_{\tau} + \gamma^s \partial_\tau^2 \boldsymbol{\eta}^*_{\tau+1} \tag{27e}$$

$$\frac{\boldsymbol{\eta}^*_{\tau+1} - \boldsymbol{\eta}^*_{\tau}}{d\tau} = \partial_\tau \boldsymbol{\eta}^*_{\tau} + d\tau\big((\frac{1}{2}-\beta^s)\partial_\tau^2 \boldsymbol{\eta}^*_{\tau} + \beta^s \partial_\tau^2 \boldsymbol{\eta}^*_{\tau+1}\big) \tag{27f}$$

$$\alpha_m^s = \frac{2\rho_\infty - 1}{\rho_\infty + 1};\ \alpha_f^s = \frac{\rho_\infty}{\rho_\infty + 1};\ \gamma^s = \frac{1}{2} - \alpha_m^s + \alpha_f^s;\ \beta^s = \frac{1}{4}(1 - \alpha_m^s + \alpha_f^s)^2 \tag{27g}$$

where the α_m^s, α_f^s, γ^s and β^s are defined to ensure the time integration scheme is unconditionally stable and second order accurate [37]. Similar to the implementation of generalized-α scheme for heat & mass transfer, the ρ_∞ represents the spectral radius to control the frequency damping.

Therefore, the structural equation at two consecutive time steps can be written as

$$\boldsymbol{M} \cdot \partial_\tau^2 \boldsymbol{\eta}^*_{\tau} + \boldsymbol{C} \cdot \partial_\tau \boldsymbol{\eta}^*_{\tau} + \boldsymbol{K} \cdot \boldsymbol{\eta}^*_{\tau} = \boldsymbol{F}_{\tau} \tag{28a}$$

$$\boldsymbol{M} \cdot \partial_\tau^2 \boldsymbol{\eta}^*_{\tau+1} + \boldsymbol{C} \cdot \partial_\tau \boldsymbol{\eta}^*_{\tau+1} + \boldsymbol{K} \cdot \boldsymbol{\eta}^*_{\tau+1} = \boldsymbol{F}_{\tau+1} \tag{28b}$$

Inserting Eq. (27e) into Eq. (27f), and subsequently substituting Eqs. (28) and (27f) into Eq. (27e), the structural velocity ($\partial_\tau \boldsymbol{\eta}^*_{\tau+1}$) at the next time step can be computed in Eq. (29). Once $\partial_\tau \boldsymbol{\eta}^*_{\tau+1}$ is obtained, the structural acceleration and displacement can be computed in Eqs. (27e) and (27f) respectively.

$$\begin{aligned}
\hat{\boldsymbol{M}} \cdot \boldsymbol{\partial}_\tau \boldsymbol{\eta}^*_{\tau+1} &= \hat{\boldsymbol{R}}_{\tau,\tau+1} \\
\hat{\boldsymbol{M}} &= \boldsymbol{M} + \gamma^s d\tau \boldsymbol{C} + \beta^s d\tau^2 \boldsymbol{K} \\
\hat{\boldsymbol{R}}_{\tau,\tau+1} &= d\tau\big[(1-\gamma^s)\boldsymbol{F}_{\tau} + \gamma^s \boldsymbol{F}_{\tau+1}\big] \\
&\quad + \big[\boldsymbol{M} - (1-\gamma^s)d\tau \boldsymbol{C} - (\gamma^s - \beta^s)d\tau^2 \boldsymbol{K}\big] \cdot \partial_\tau \boldsymbol{\eta}^*_{\tau} \\
&\quad - d\tau \boldsymbol{K} \cdot \boldsymbol{\eta}^*_{\tau} - \gamma^s d\tau^3 \big[\frac{1}{2} - \beta^s - \frac{(1-\gamma^s)\beta^s}{\gamma^s}\big] \boldsymbol{K} \cdot \partial_\tau^2 \boldsymbol{\eta}^*_{\tau}
\end{aligned} \tag{29}$$

Due to the complicated interaction between fluid, heat and species, it is expected that the multiple scales in heat & mass transfer can lead to very small time step. This restriction of time step increases the computational cost in practice, especially for the implicit time integration schemes and the multi-scale simulations. In this study, the double diffusive mixed convection flow over a stationary circular cylinder is taken as an example to assess the performance of the implemented generalized-α scheme. In this configuration, the cylinder possesses the highest temperature ($\theta = 1.0$) and concentration of species ($C = 1.0$). The size of the computational domain is $60L \times 50L$, where L is the cylinder's diameter. The upstream and side distances respectively are $20L$ and $25L$. The values of the dimensionless groups are $Re = 100$, $Pr = 0.7$, $Br = 1.0$ and $Le = 5.0$. Thanks to the robust generalized-α time integration scheme, the time convergence study in Table 1 shows that the results converge at $d\tau = 0.005$ (the error is within 1%). In fact, except for the fluctuation of lift force (C_l^{rms}), who error is about 1.2% with respect to the referential values, the errors of the other results at $d\tau = 0.01$ are also within 1%.

Table 1
Double-diffusive mixed convection over a circular cylinder at $Re = 100$, $Pr = 0.7$, $Ri = 1.0$, $Br = 1.0$, $Le = 5.0$ and different time steps.

TIME STEP	$\overline{C_d}$	$\overline{C_l}$	C_l^{rms}	$\overline{Nu}$	Nu^{rms}	$\overline{Sh}$	Sh^{rms}
$d\tau = 0.0400$	1.194	−1.782	0.295	5.221	0.055	9.692	0.139
	(1.6%)	(2.6%)	(10.9%)	(0.5%)	(0.0%)	(0.4%)	(3.5%)
$d\tau = 0.0200$	1.204	−1.807	0.311	5.235	0.055	9.716	0.142
	(0.8%)	(1.2%)	(6.0%)	(0.3%)	(0.0%)	(0.2%)	(1.4%)
$d\tau = 0.0100$	1.211	−1.818	0.327	5.242	0.055	9.728	0.143
	(0.2%)	(0.6%)	(1.2%)	(0.1%)	(0.0%)	(0.0%)	(0.7%)
$d\tau = 0.0050$	1.213	−1.825	0.330	5.248	0.055	9.732	0.144
	(0.0%)	(0.2%)	(0.3%)	(0.0%)	(0.0%)	(0.0%)	(0.0%)
$d\tau = 0.0025$	1.214	−1.829	0.331	5.249	0.055	9.734	0.144

In the proposed numerical formulation, a second-order accurate staggered-partitioned scheme [38] is employed to couple the fluid and the structure equations. The pseudocode of the implemented fluid–structure coupling scheme in each time step is briefly summarized below

In each time step (t):

1. predict the traction force on the structure: $\boldsymbol{h}_p^{*cyl}(t+1) = 2\,\boldsymbol{h}^{*cyl}(t) - \boldsymbol{h}^{*cyl}(t-1)$
2. find the solution to the structure equation for the next time step, $\partial_\tau \boldsymbol{\Phi}^*(t+1)$ and $\boldsymbol{\eta}^*(t+1)$
3. update the location and velocity of the structure in fluid and find the solution to fluid equation for the next time step, $\boldsymbol{u}^*(t+1)$ and $\hat{\boldsymbol{h}}^*(t+1)$
4. relax the traction force along interface $\Gamma^{fs}(t+1)$: $\boldsymbol{h}^{*cyl}(t+1) = -\gamma^{fs}\hat{\boldsymbol{h}}^*(t+1) + (1-\gamma^{fs})\boldsymbol{h}_p^{*cyl}(t+1)$

where γ^{fs} is the relaxation parameter. In this study, $\gamma^{fs} = 0.8$ is used for all numerical examples. The predicted traction force at the next time step ($\boldsymbol{h}_p^{*cyl}(t+1)$) is a first-order approximation. The relationship between the traction forces experienced by the structure and the fluid is $\boldsymbol{h}^{*cyl}(t) = -\boldsymbol{h}^*(t)$. For the detailed algorithm of this coupling scheme and the second-order predicted traction force, please refer to Dettmer & Perić (2013) [38].

4. Numerical examples

The accuracy and robustness of the proposed numerical formulation are assessed by studying a number of numerical examples, e.g., forced convection, mixed convection, heat & mass transfer, rotation, vibration and cylinder arrays. Except for the validation cases, in all numerical examples, (a) the stabilized Nitsche's method is employed; (b) the Ghost penalty parameter is set as 0.01; (c) the relaxation parameter in fluid–structure coupling is 0.8 and (d) the mass ratio and the damping ratio are $m^* = 10$ and $\zeta = 0.01$ respectively, unless otherwise specified. The numerical results are compared with the other numerical results, experiments and an empirical correlation in literature.

4.1. Heat convection

For the simulations of heat convection, the conservation of species is completely decoupled with the Navier–Stokes equation and the conservation of energy. Except for the simulation of heat & mass transfer within an enclosure in Section 4.2.1, the numerical examples of cylinders are simulated in three configurations: (a) a fixed/rotating cylinder; (b) a vibrating cylinder and (c) three fixed/vibrating cylinders in an equilateral-triangular arrangement, as shown in Fig. 4, where L_u, L_d, H, L, a and g^* respectively are the upstream distance, the downstream distance, the height of domain, the characteristic length (the cylinder's diameter), the angular speed of a cylinder and the center-to-center distance of cylinders. For the simulation of a fixed heated cylinder, the value of angular velocity is taken as zero ($a = 0.0$). In Fig. 4(c), the cylinder upstream is cylinder 1, the top cylinder downstream is cylinder 2 and the last one is cylinder 3.

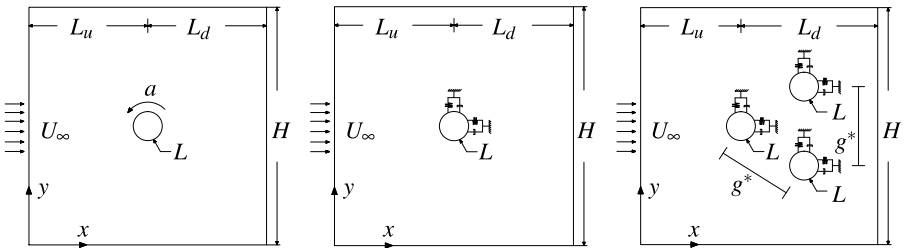

Fig. 4. Schematic diagrams of cylinder(s): (a) a fixed/rotating heated cylinder; (b) a vibrating heated cylinder and (c) vibrating heated cylinders in equilateral-triangular arrangement.

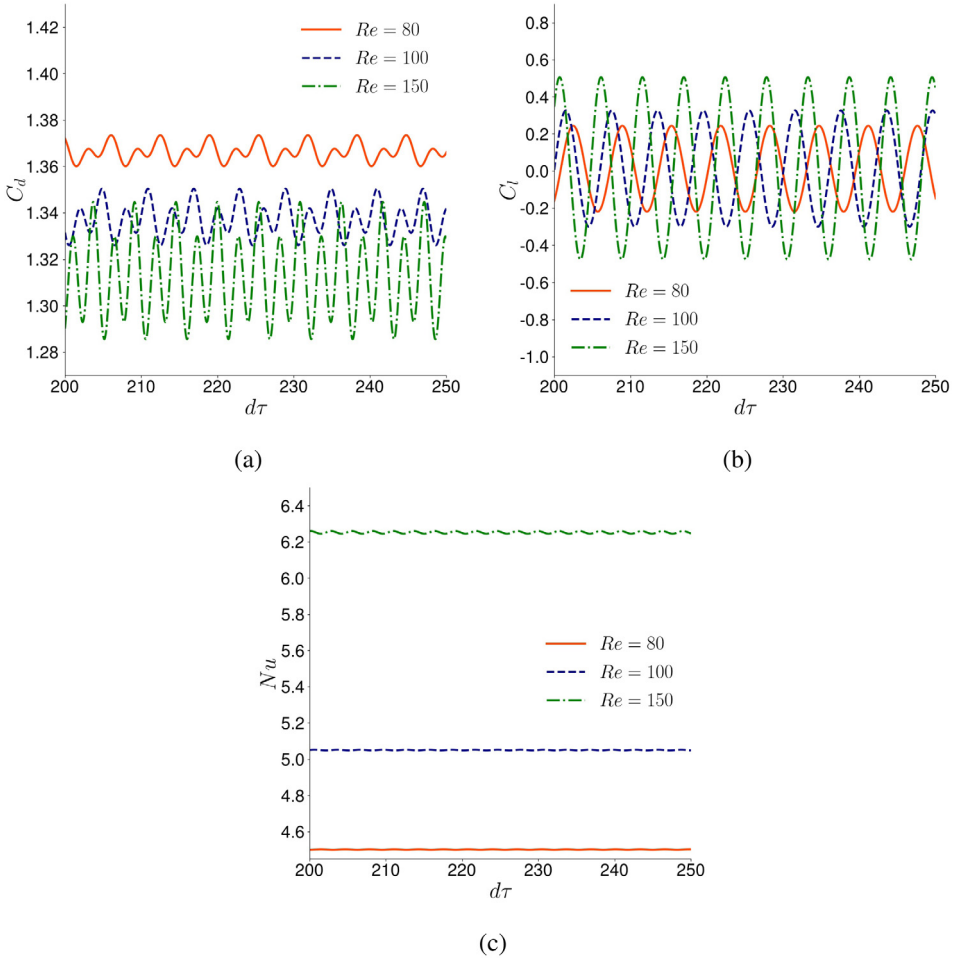

Fig. 5. Forced convection over a heated cylinder at $Re = [80, 150]$ and $Pr = 0.7$: (a) drag coefficient; (b) lift coefficient and (c) averaged Nusselt number.

The boundary conditions ($u^* = U_\infty = 1.0$, $v^* = \theta = C = 0.0$) are imposed along the inlet, the left boundary of the computational domain. The traction-free boundary condition is imposed along the other boundaries of domain,

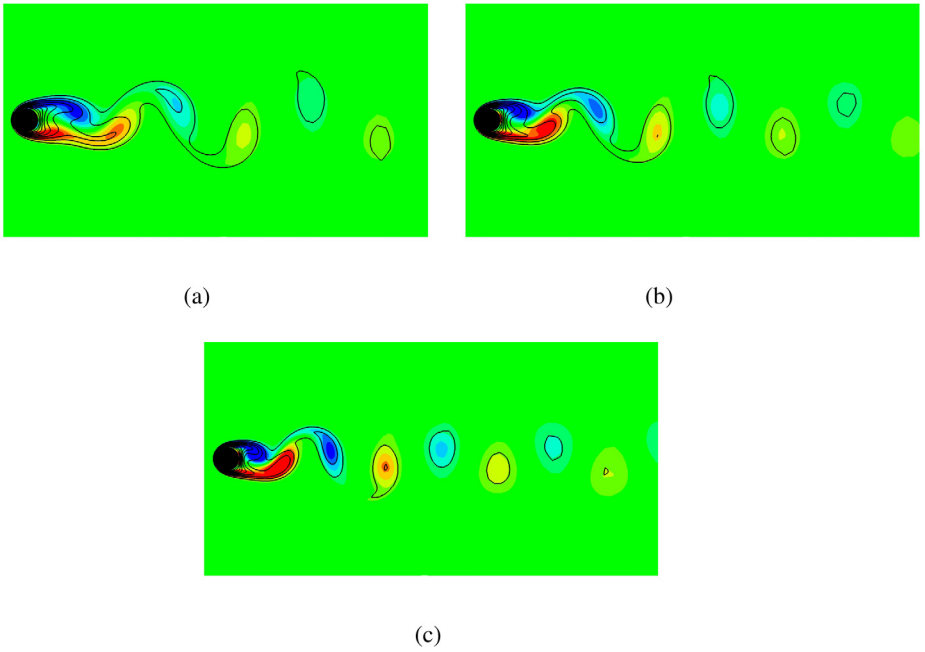

Fig. 6. Contours of vorticity and temperature for forced convection over a heated cylinder at $Pr = 0.7$ and $\tau = 250$: (a) $Re = 80$; (b) $Re = 100$ and (c) $Re = 150$. The plots are colored with vorticity contours ($\omega \in [-2.0, 2.0]$) and the solid lines are temperature contours ($\theta \in [0, 1.0]$).

Table 2
Time-averaged Nusselt number ($\overline{Nu}$) for forced convection over a heated cylinder.

Pr	1.0			10		
Re	10	20	30	10	20	30
Churchill & Bernstein [39]	2.062	2.793	3.355	4.414	6.123	7.435
Juncu [40]	2.061	2.727	3.229	4.260	5.740	6.944
Sarkar et. al. [41]	2.078	2.753	3.238	4.303	5.775	7.012
Liu [42]	2.060	2.715	3.201	4.284	5.699	6.971
Present	2.061	2.721	3.217	4.329	5.762	6.991

e.g., the outlet and the sides. The Dirichlet boundary condition ($\theta = C = 1.0$) is weakly satisfied by the Nitsche's method along the embedded cylinder(s).

4.1.1. Forced and mixed convection over a heated cylinder

The forced convection over a fixed cylinder is a classical benchmark example used to study the performance of a numerical scheme. The geometry and boundary conditions, $L_u = 20$, $L_d = 50$, $H = 50$, $L = 1.0$, $U_\infty = 1.0$ and $a = 0.0$ (fixed cylinder), for this problem are shown in Fig. 4(a). The total number of elements is 34 271 and there are 60 elements across the diameter of cylinder. The time step taken is $\partial\tau = 0.01$.

The cases of forced convection ($Ri = 0.0$) are studied at first. The computed time-averaged Nusselt number ($\overline{Nu}$) for a fixed cylinder in forced convection at different Re and Pr values are compared with literature in Table 2. Similarly, the hydrodynamic forces obtained from the proposed numerical formulation are also validated with those from literature in Table 3 for unsteady flow over a fixed heated cylinder at $Re = [100, 200]$ and $Pr = 0.7$. These computed numerical results show good agreement with numerical simulations in literature. Furthermore, the computed values of $\overline{Nu}$ match well with the empirical correlation for forced convection [39] in Tables 2 and 3 too.

The empirical correlation [39] to approximate the averaged Nusselt number in forced convection over a heated cylinder is defined in Eq. (30) and used in Tables 2 and 3. It is calibrated with experimental data and recommended

Table 3
Forced convection over a heated cylinder at $Re = [100, 200]$ and $Pr = 0.7$.

Re	Reference	C_d	C_l	St	Nu
100	Churchill & Bernstein [39]	–	–	–	5.16
	Liu et. al. [43]	1.350 ± 0.012	± 0.339	0.164	–
	Mahir & Altaç [44]	1.368 ± 0.029	± 0.343	0.172	5.179 ± 0.003
	Izadpanah et. al. [45]	1.373 ± 0.010	± 0.229	0.169	5.159 ± 0.002
	Present	1.342 ± 0.012	± 0.328	0.167	5.156 ± 0.002
200	Churchill & Bernstein [39]	–	–	–	7.19
	Liu et. al. [43]	1.310 ± 0.049	± 0.690	0.192	–
	Mahir & Altaç [44]	1.376 ± 0.048	± 0.698	0.192	7.474 ± 0.028
	Izadpanah et. al. [45]	1.336 ± 0.046	± 0.700	0.200	7.452 ± 0.026
	Present	1.369 ± 0.047	± 0.690	0.192	7.441 ± 0.028

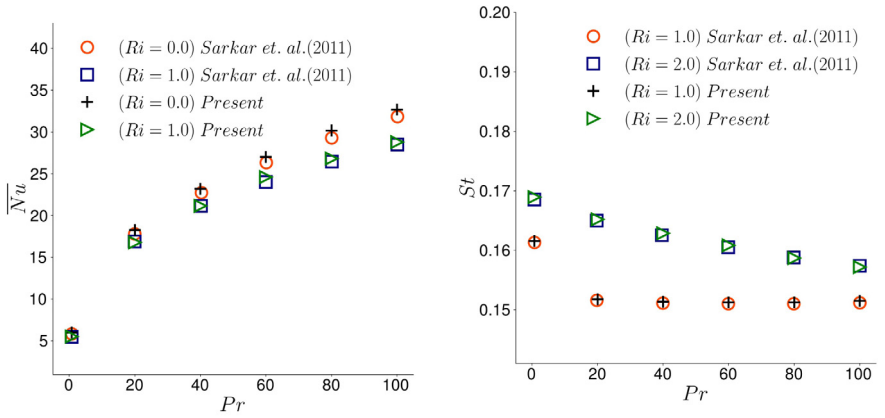

(a) (b)

Fig. 7. Mixed convection over a heated cylinder at $Re = 100$, $Pr = [0.7, 100]$ and $Ri = [0.0, 2.0]$: (a) time-averaged Nusselt number; and (b) Strouhal number.

for the cases of $Re\ Pr \gtrsim 0.2$. It shows that the approximated heat convection based on the proposed numerical scheme match well with the empirical correlation.

$$\overline{Nu} = 0.3 + \frac{0.62 Re^{1/2} Pr^{1/3}}{[1 + (0.4/Pr)^{2/3}]^{1/4}} \left[1 + \left(\frac{Re}{282000}\right)^{5/8}\right]^{4/5} \tag{30}$$

The time histories of C_d, C_l and Nu for the forced convection over a heated cylinder at $Re = [80, 150]$ and $Pr = 0.7$ are shown in Fig. 5. The obtained values of Nu match well with the results of numerical simulation and empirical correlation in Table 3. The corresponding contours of the spanwise vorticity (ω) and the temperature (θ) are plotted in Fig. 6. It can be seen that the temperature contours (the solid lines) follows closely with the dynamics of the vortices downstream (the colored contours) in forced convection.

For forced convection, the conservation of energy is completely decoupled with the Navier–Stokes equation. Whereas, the perturbation of the temperature field on fluid inertia is important in mixed convective flow. This perturbation becomes very important to vortex dynamics in wake. As shown in Fig. 7, the time-averaged Nusselt number and Strouhal number change proportionally with the Prandtl and Richardson numbers in mixed convection. The obtained results of Nu and St in Fig. 7 show good agreement with literature [46]. The time histories of C_d, C_l and Nu for the mixed convection over a heated cylinder at $Re = 100$, $Pr = [0.7, 10]$ and $Ri = [1.0, 2.0]$ are presented in Fig. 8. It is found that the buoyancy action in mixed convection has a significant influence on the hydrodynamic forces. The corresponding contours of the vorticity and the temperature are exhibited in Fig. 9.

For the cases of vibrating cylinder(s), it is assumed that there is a spring–damper system attached on cylinder(s). In this study, the natural frequencies of cylinder in streamwise and transverse directions are assumed to be identical,

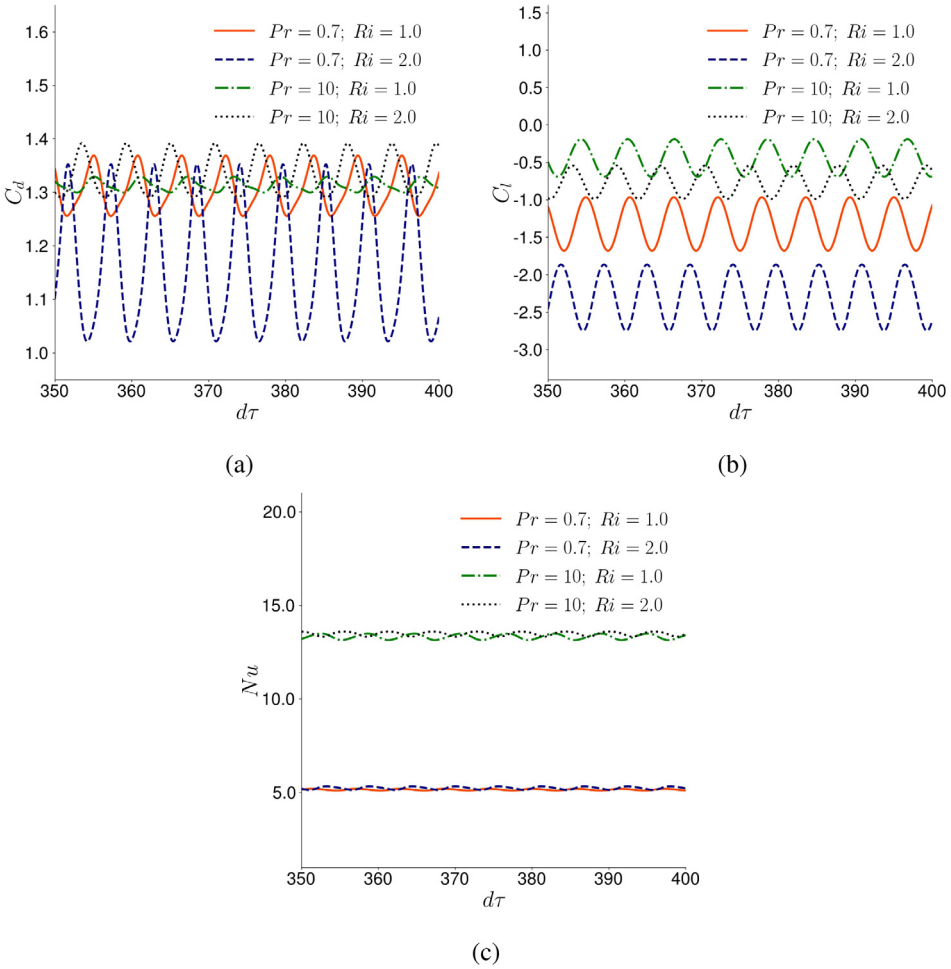

Fig. 8. Mixed convection over a heated cylinder at $Re = 100$, $Pr = [0.7, 10]$ and $Ri = [1.0, 2.0]$: (a) drag coefficient; (b) lift coefficient and (c) averaged Nusselt number.

$f_{nx} = f_{ny}$. The proposed formulation for structural vibration is validated with literature [47,48]. In validation, a 1-Degree-of-Freedom (DOF) vibrating heated cylinder in forced convection is simulated. In this case, the Reynolds number, the Prandtl number, the mass ratio, the damping ratio respectively are set as $Re = 150$, $Pr = 0.7$, $m^* = 2.0$ and $\zeta = 0.0$. The time-averaged Nusselt number ($\overline{Nu}$) and the transverse vibration (A_y) are chosen for comparison in Fig. 10, which shows a good agreement between the obtained numerical results and literature. The corresponding contours of vorticity and velocity magnitude of a 1-DoF heated cylinder vibrating in transverse direction are shown in Fig. 11. These validation cases show that the proposed numerical formulation is robust and accurate to approximate the complex situations in multi-physics simulations involving heat convection and fluid–structure interaction.

4.1.2. Forced and mixed convection over an equilateral-triangular arrangement

The proximity and the wake interference in multi-body systems are strong. Hence, the heat convection, the hydrodynamics and the boundary layer dynamics are much more complicated. It imposes a challenge to unfitted finite element formulations to accurately approximate the complicated variation in boundary layers and vorticity clusters in near wake. To this end, three heated cylinders in an equilateral-triangular arrangement at a typical gap distance $g^* = 3.0$ is chosen to assess the robustness of the proposed Nitsche's method and the PAGQ numerical integration scheme.

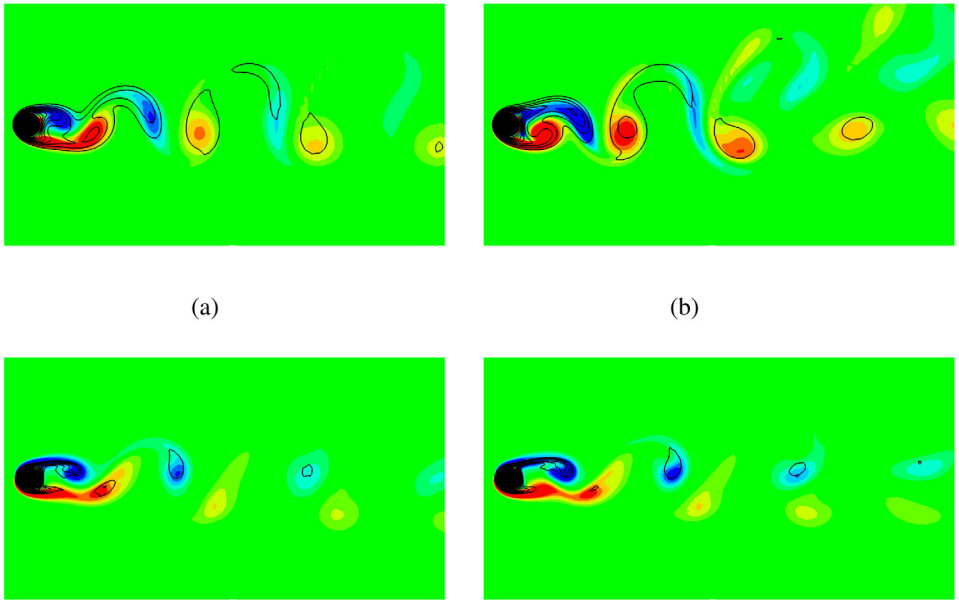

Fig. 9. Contours of vorticity and temperature for mixed convection over a heated cylinder at $Re = 100$ and $\tau = 350$: (a) $Pr = 0.7$ and $Ri = 1.0$; (b) $Pr = 0.7$ and $Ri = 2.0$; (c) $Pr = 10$ and $Ri = 1.0$ and (d) $Pr = 10$ and $Ri = 2.0$. The plots are colored with vorticity contours ($\omega \in [-2.0, 2.0]$) and the solid lines are temperature contours ($\theta \in [0, 1.0]$).

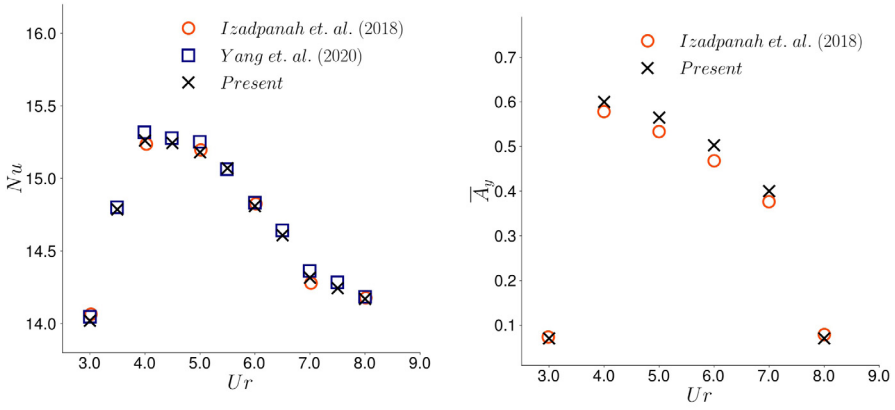

Fig. 10. Forced convection over a 1-DoF vibrating cylinder at $Re = 150$, $Pr = 0.7$, $m^* = 2.0$ and $\zeta = 0.0$: (a) time-averaged Nusselt number; and (b) transverse vibration.

In this study, the case of forced convection over an equilateral-triangular arrangement at $Re = 100$, $Pr = 0.7$ and $g^* = 3.0$ is chosen for the purpose of validation. The total number of element for the cases of equilateral-triangular arrangement is 82 471. There are 60 elements along the diameter of each cylinder and the growth rate of element is controlled within 1.05. As listed in Table 4, the results obtained with the present scheme agree well with literature [49–51], where the subscripts (1 and 2) refer to the cylinder upstream and the top cylinder downstream. $\Delta(\cdot)$ indicate the fluctuation of a quantity, e.g., ΔC_d means the fluctuation of drag coefficient with respect to its time-averaged value. The corresponding contours of the spanwise vorticity, the temperature and the

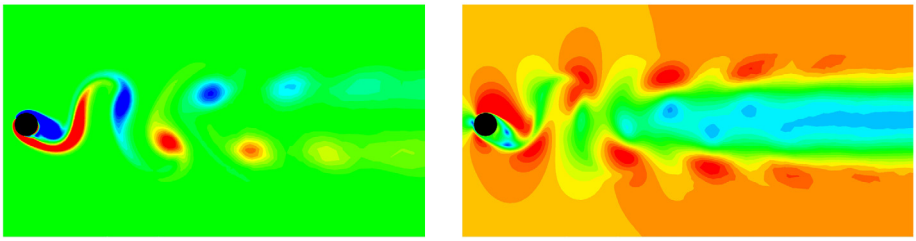

(a) (b)

Fig. 11. Contours for forced convection over a vibrating heated cylinder at $Re = 150$, $Pr = 0.7$, $m^* = 2.0$, $\zeta = 0.0$ and $\tau = 350$: (a) vorticity field ($\omega \in [-2.0, 2.0]$) and (b) velocity magnitude ($|\boldsymbol{u}^*| \in [0.0, 1.2]$).

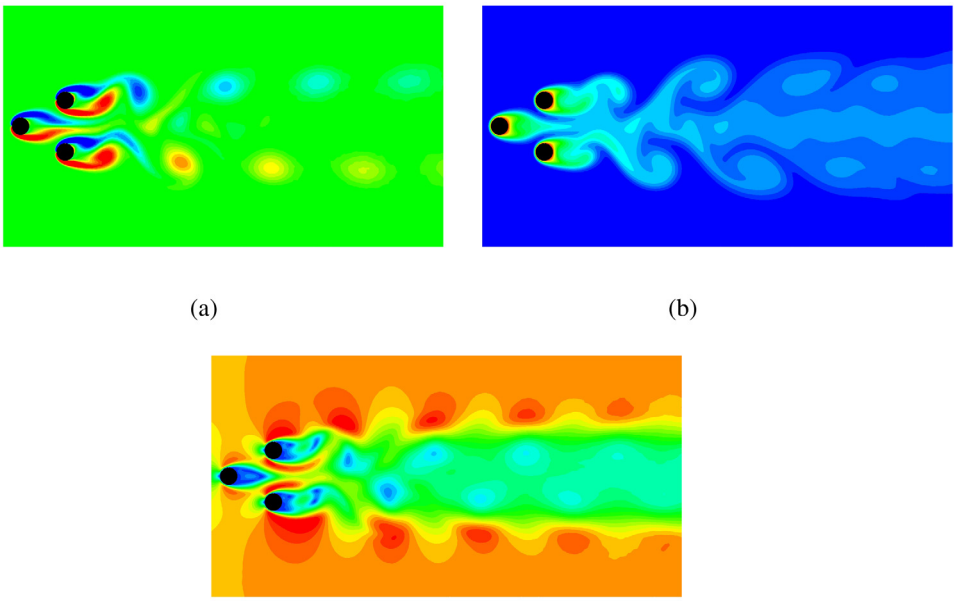

(a) (b)

(c)

Fig. 12. Contours for forced convection over an equilateral-triangular arrangement at $Re = 100$, $Pr = 0.7$, $g^* = 3.0$ and $\tau = 400$: (a) vorticity field ($\omega \in [-2.0, 2.0]$); (b) temperature field ($\theta \in [0.0, 1.0]$) and (c) velocity magnitude ($|\boldsymbol{u}^*| \in [0.0, 1.2]$).

Table 4
Forced convection over an equilateral-triangular arrangement at $Re = 100$, $Pr = 0.7$ and $g^* = 3.0$.

	$\overline{C}_{d1}$	ΔC_{d1}	$\overline{C}_{l1}$	ΔC_{l1}	$\overline{C}_{d2}$	ΔC_{d2}	$\overline{C}_{l2}$	ΔC_{l2}	St
Bao et. al. [49]	1.05	0.0010	0	0.0175	1.26	0.0167	−0.060	0.201	–
Zheng et. al. [50]	1.23	0.0288	0	−0.002	1.53	0.0214	−0.087	0.335	–
Chen et. al. [51]	1.03	0.0014	0	0.0173	1.23	0.0166	−0.059	0.181	0.137
Present	1.02	0.0011	0	0.0174	1.22	0.0210	−0.057	0.205	0.137

velocity magnitude are presented in Fig. 12. Due to the enhanced proximity and wake interference, a complicated interaction of temperature field is observed in wake in Fig. 12(b).

In mixed convection, the influence of thermal buoyancy is important. Especially, the amplified perturbation from the buoyancy-driven flow also imposes a numerical challenge on the embedded-interface formulations, because of

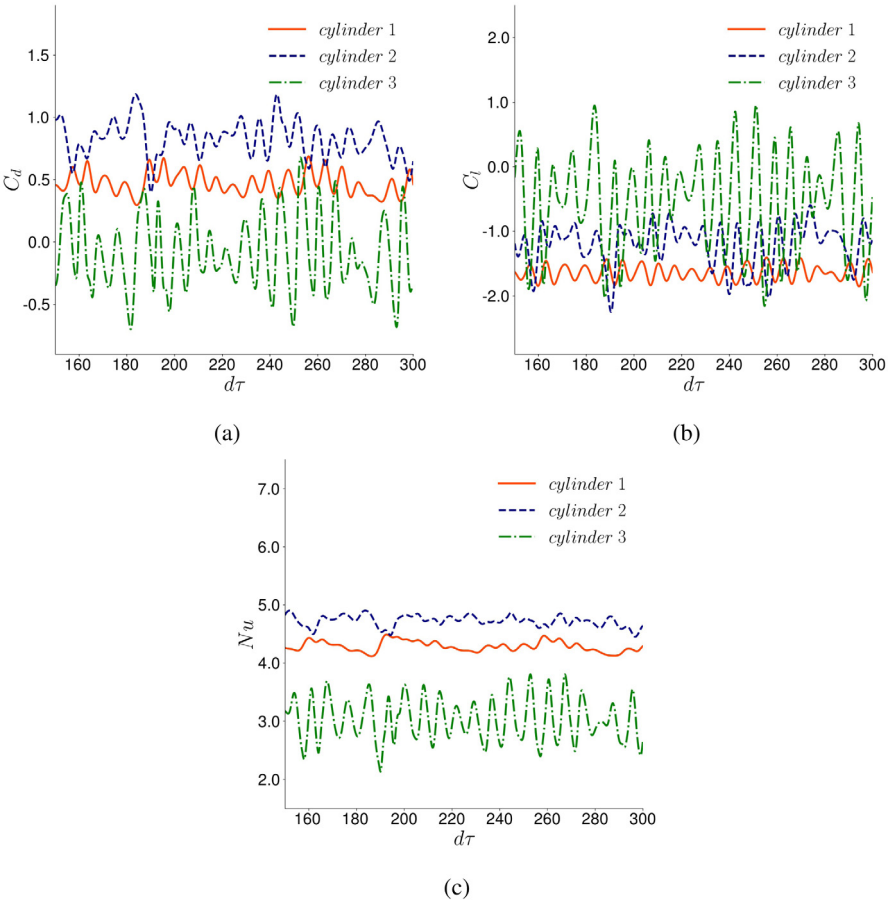

Fig. 13. Mixed convection over an equilateral-triangular arrangement at $Re = 100$, $Pr = 0.7$, $Ri = 1.0$ and $g^* = 3.0$: (a) drag coefficient; (b) lift coefficient and (c) averaged Nusselt number.

the strong temperature gradient. A case of mixed convection over an equilateral-triangular arrangement at $Re = 100$, $Pr = 0.7$, $Ri = 1.0$ and g^* is also chosen to assess the robustness of the proposed scheme. The time histories of C_d, C_l and Nu from three heated cylinders are plotted in Fig. 13.

It is found that the nonlinearity in hydrodynamic responses is very strong due to the proximity and the wake interference. Especially, cylinder 3 experiences the strongest fluctuation in hydrodynamic forces and heat convection. The corresponding contours of the spanwise vorticity, the temperature, the pressure and the velocity magnitude are plotted in Fig. 14. Compared with Fig. 12 in forced convection, the wake in Fig. 14 is non-symmetric due to cross thermal buoyancy. The overall temperature around the cylinder 3 is high in Fig. 14(b), which indicates a smaller temperature gradient and inefficiency of heat convection. A large recirculating region of low pressure is also observed around the cylinder 3 in Fig. 14(c). It explains the large fluctuation of the hydrodynamic forces around the cylinder 3 in Fig. 13.

4.2. Heat and mass transfer

In heat & mass transfer, both the conservation of energy and species are fully coupled with the Navier–Stokes equation. Two additional dimensionless groups are introduced for heat & mass transfer: they are the buoyancy ratio (Br) and the Lewis number (Le). For example, if the density of the species is assumed to be higher than that of the mixture, the fluid is weighed down as the species concentration increases. This results in β_c and Br being negative values and vice versa. On the other hand, the Lewis number also indicates the strength of the species diffusivity

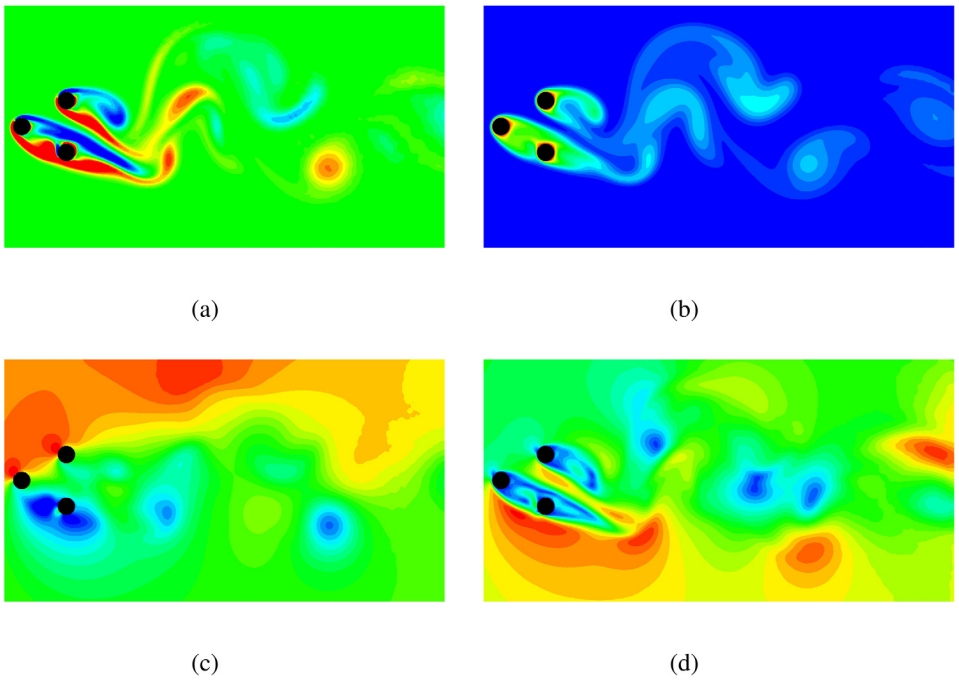

Fig. 14. Contours for mixed convection over an equilateral-triangular arrangement at $Re = 100$, $Pr = 0.7$, $Ri = 1.0$, $g^* = 3.0$ and $\tau = 200$: (a) vorticity field ($\omega \in [-2.0, 2.0]$); (b) temperature field ($\theta \in [0.0, 1.0]$); (c) pressure field ($p^* \in [-1.2, 0.4]$) and (d) velocity magnitude ($|\boldsymbol{u}^*| \in [0.0, 1.8]$).

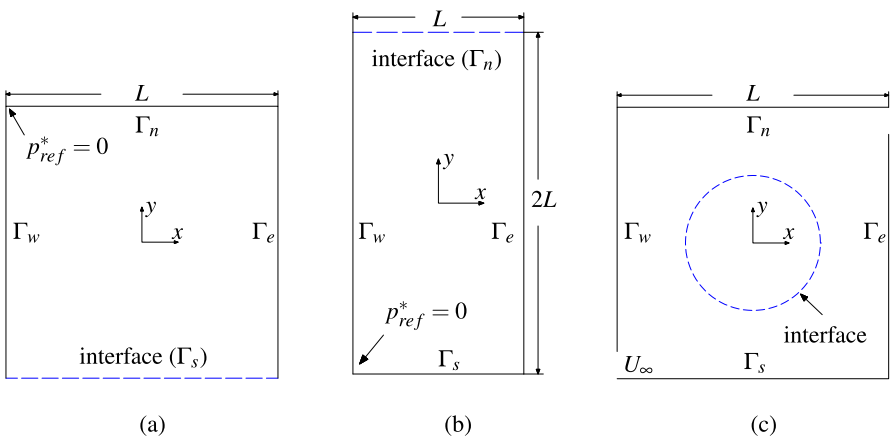

Fig. 15. Schematic diagrams of heat & mass transfer in enclosures: (a) binary gases in an enclosure; (b) heat & mass transfer in lid-driven cavity flow and (c) double-diffusive mixed convection around a heated cylinder in an enclosure.

with respect to the thermal diffusivity. In this study, the proposed scheme is assessed for both the positive and the negative values of Br and a range of Lewis numbers.

4.2.1. Double-diffusive mixed convection in an enclosure

The proposed scheme for heat & mass transfer is validated with the simulations and the experiment in literature. Three configurations are considered: (a) binary gases in an enclosure in Fig. 15(a); (b) heat & mass transfer in lid-driven cavity flow in Fig. 15(b) and (c) double-diffusive mixed convection around a heated cylinder in an

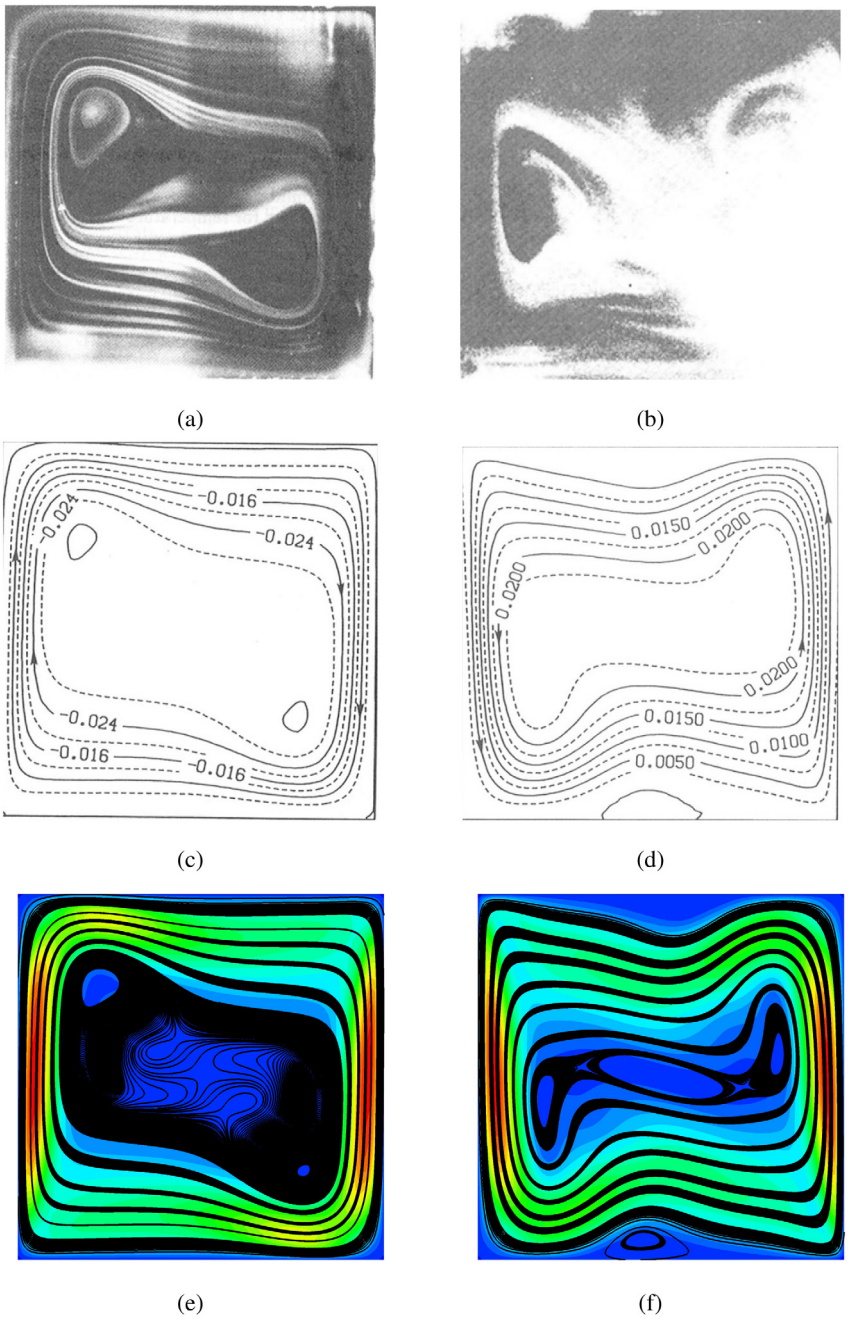

Fig. 16. Comparison of streamlines for heat & mass transfer of binary gases in an enclosure: (a) experiment at $Ri = 1.0$, $Gr = 5.88 \times 10^5$, $Br = 0.55$ and $Le = 0.588$; (c,e) simulations at $Ri = 1.0$, $Gr = 5.91 \times 10^5$, $Br = 0.55$ and $Le = 0.588$; (b) experiment at $Ri = 1.0$, $Gr = 9.31 \times 10^5$, $Br = -1.85$ and $Le = 0.823$ and (d, f) simulations at $Ri = 1.0$, $Gr = 9.27 \times 10^5$, $Br = -1.85$ and $Le = 0.823$. Fig. 16(a,b,c,d) are obtained in literature [52].

enclosure in Fig. 15(c). $L = 1.0$ is the characteristic length. $p^*_{ref} = 0.0$ is a referential pressure imposed at a node in fluid boundary. The origin of the coordinate system is placed in the center of computational domains in Fig. 15. The embedded interface is highlighted with dotted blue lines, where the proposed Nitsche's method is employed.

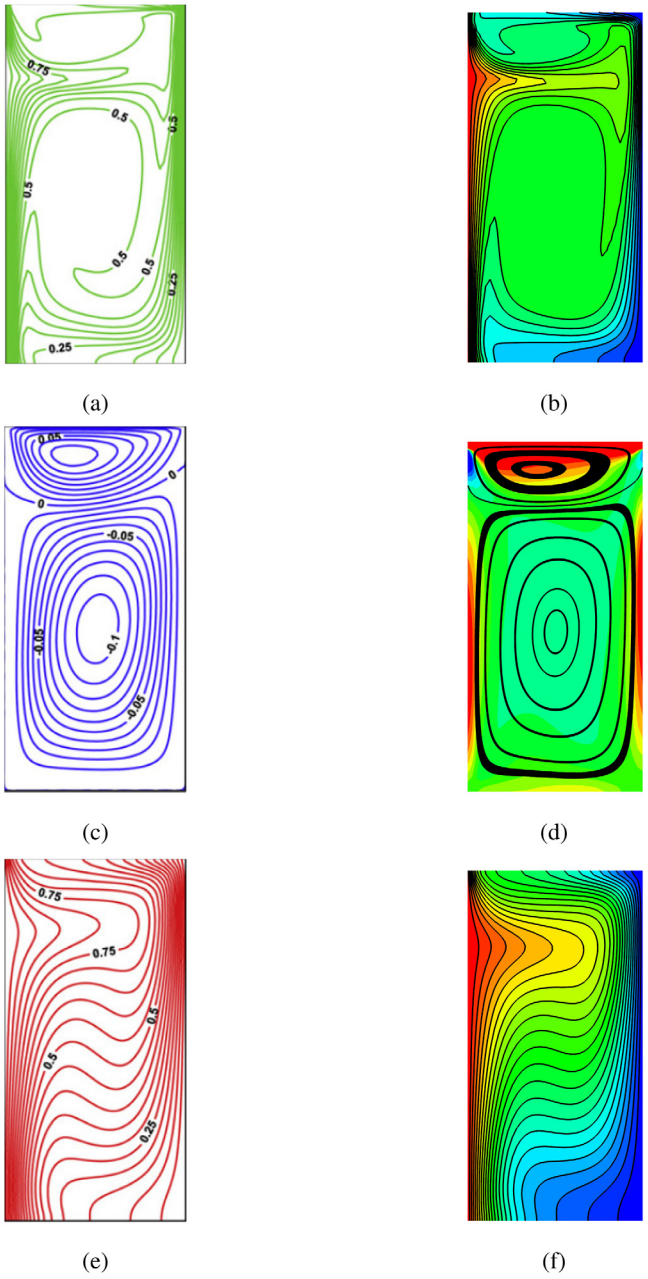

Fig. 17. Double-diffusive mixed convection in a rectangular enclosure with an insulated moving lid at $Pr = 0.7$, $Ri = 1.0$, $Br = 1.0$, $Le = 10.0$ and $u^*_{lid} = -1.0$: (a,b) iso-concentration lines of species; (c,d) streamlines and (e,f) iso-thermal lines. Fig. 17(a,c,e) are obtained in literature [53].

For the configuration (a) in Fig. 15(a), the following boundary conditions are imposed along the boundaries.

- $\boldsymbol{u}^* = 0.0;\ \theta = C = 1.0 \quad \forall \boldsymbol{x} \in \Gamma_w$
- $\boldsymbol{u}^* = 0.0;\ \theta = C = 0.0 \quad \forall \boldsymbol{x} \in \Gamma_e$
- $\boldsymbol{u}^* = 0.0;\ \theta = 1.0 - (x + 0.5);\ C = 0.0 \quad \forall \boldsymbol{x} \in \Gamma_n \cup \Gamma_s$

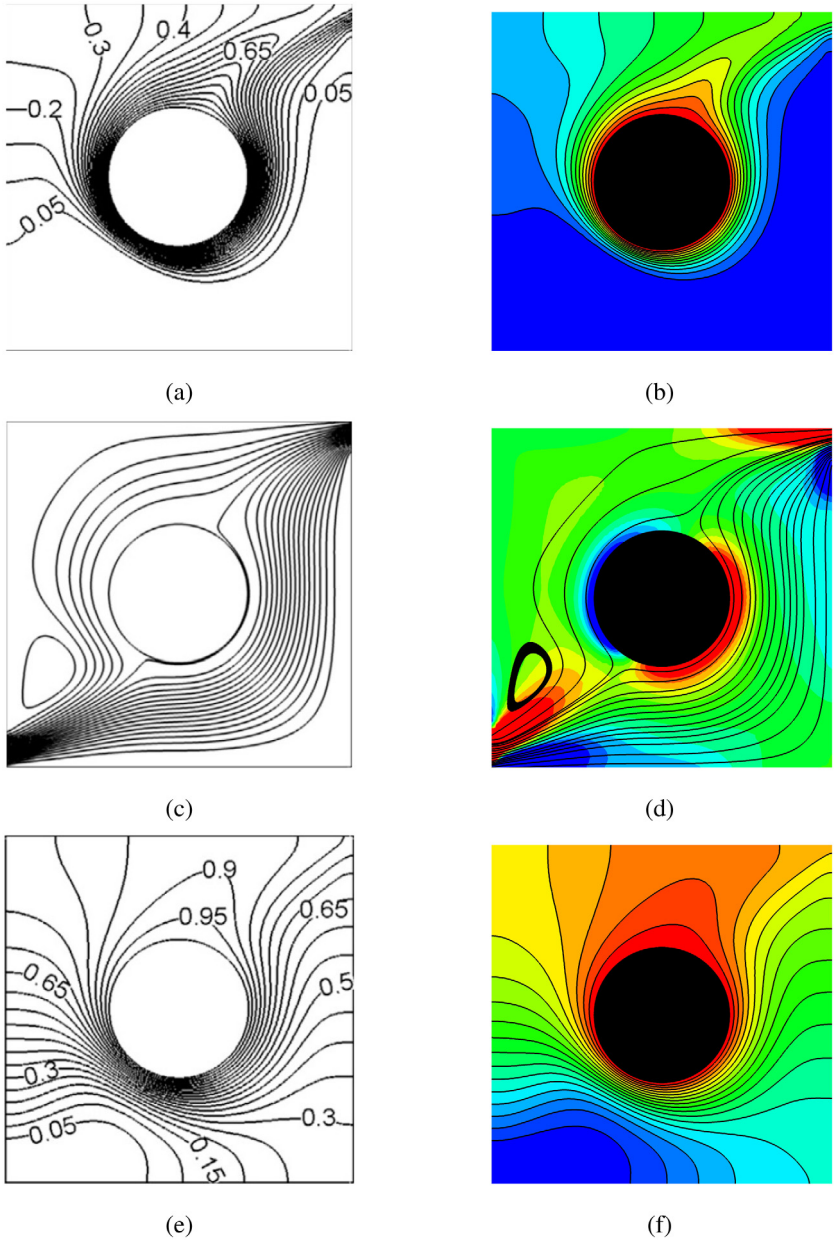

Fig. 18. Double-diffusive mixed convection over a heated cylinder in a square enclosure at $Gr = 1.4 \times 10^4$, $Ri = 1.0$, $Pr = 0.7$, $Br = 1.0$ and $Le = 5.0$: (a,b) iso-concentration lines of species; (c,d) streamlines and (e,f) iso-thermal lines. Fig. 18(a,c,e) are obtained in literature [54].

The total number of elements for the configuration (a) is 6400. The time step is $d\tau = 0.01$. The results obtained for the configuration (a) are presented in Fig. 16(e,f) and compared with the experiments and simulations in literature [52] in Fig. 16(a,b,c,d). The detailed setup of the parameters are stated in the caption of Fig. 16. It is found that the results obtained from the proposed formulation match well with the experimental and numerical data in literature [52].

Next, the proposed scheme is assessed in configuration (b), the heat & mass transfer in lid-driven cavity flow, as shown in Fig. 15(b). The following boundary conditions are imposed along the boundaries of the configuration (b).

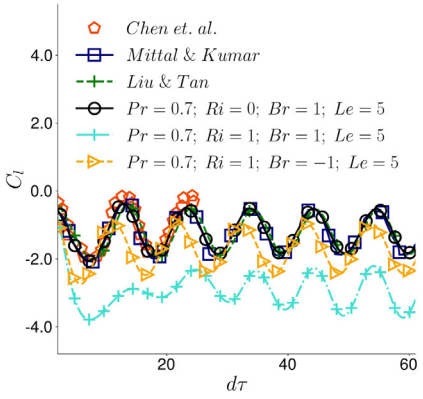

Fig. 19. Lift coefficient of a rotating heated disk in double-diffusive mixed convection at $Re = 200$, $Pr = 0.7$, $Ri = [0.0, 1.0]$, $Br = [-1.0, 1.0]$, $Le = 5.0$ and $a = 1.0$.

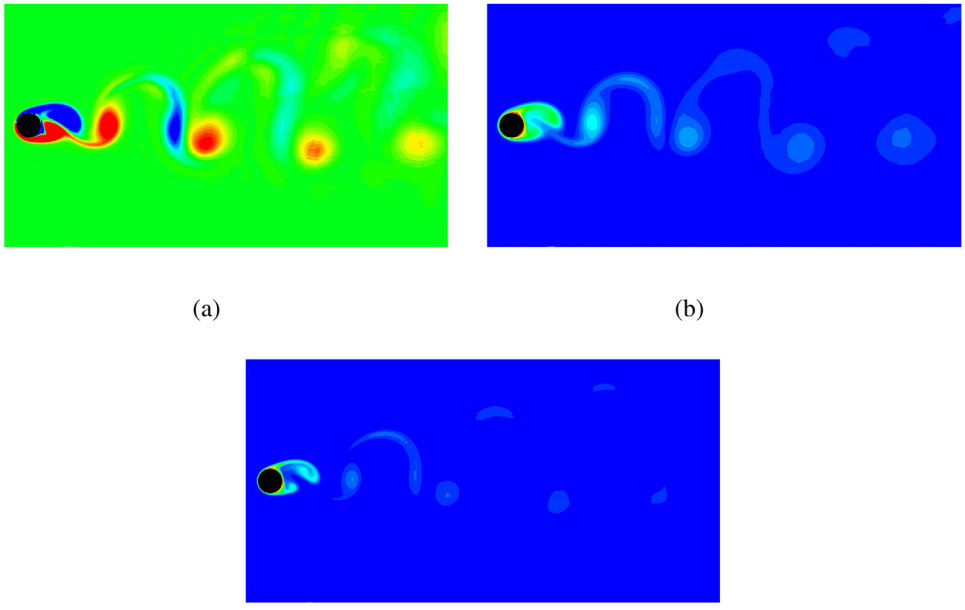

Fig. 20. Contours for double-diffusive mixed convection over a rotating heated disk at $Re = 200$, $Pr = 0.7$, $Ri = 1.0$, $Br = 1.0$, $Le = 5.0$, $a = 1.0$ and $\tau = 50$: (a) vorticity field ($\omega \in [-2.0, 2.0]$); (b) temperature field ($\theta \in [0.0, 1.0]$) and (c) species field ($C \in [0.0, 1.0]$).

- $\boldsymbol{u}^* = 0.0;\ \theta = C = 1.0 \quad \forall \boldsymbol{x} \in \Gamma_w$
- $\boldsymbol{u}^* = 0.0;\ \theta = C = 0.0 \quad \forall \boldsymbol{x} \in \Gamma_e$
- $u^* = -1.0;\ v^* = 0.0;\ \frac{\partial \theta}{\partial \boldsymbol{n}} = \frac{\partial C}{\partial \boldsymbol{n}} = 0.0 \quad \forall \boldsymbol{x} \in \Gamma_n$
- $\boldsymbol{u}^* = 0.0;\ \frac{\partial \theta}{\partial \boldsymbol{n}} = \frac{\partial C}{\partial \boldsymbol{n}} = 0.0 \quad \forall \boldsymbol{x} \in \Gamma_s$

where $p^*_{ref} = 0.0$ is a referential pressure imposed on one node along boundary Γ_w. The stabilized Nitsche's method is applied along boundary Γ_n. The total number of element and the time step taken are 12 800 and 0.01 respectively. The obtained results are compared with literature [53] in Fig. 17. The contours in Fig. 17(d) are

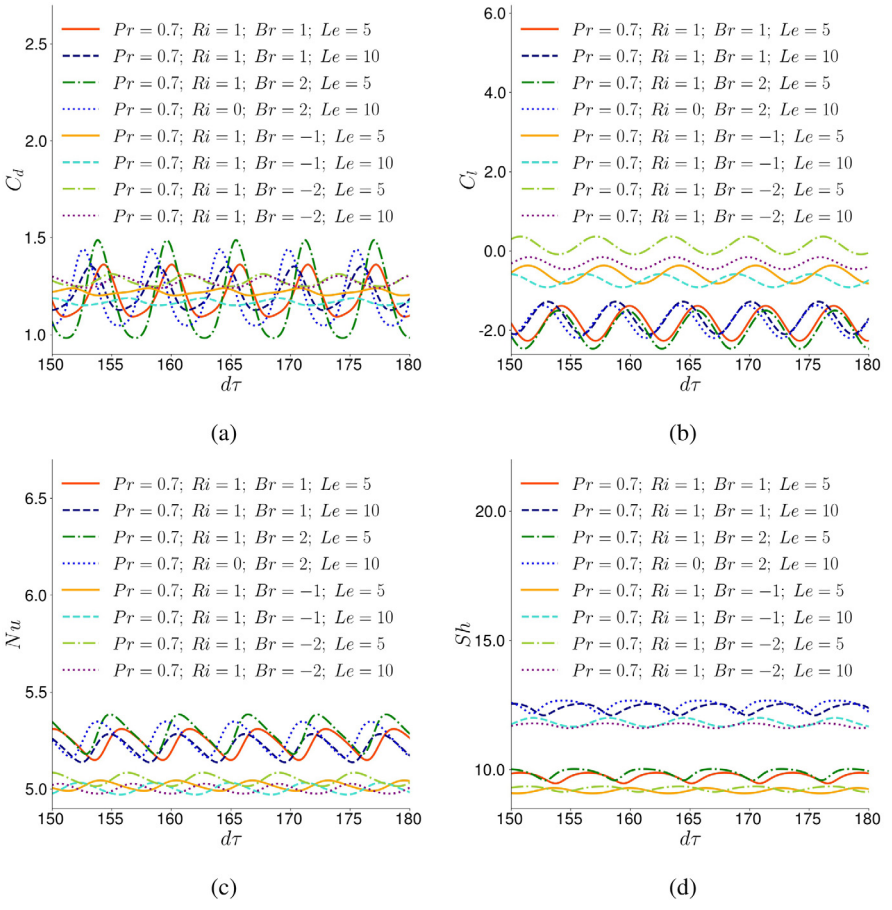

Fig. 21. Double-diffusive mixed convection over a heated cylinder at $Re = 100$, $Pr = 0.7$, $Ri = 1.0$, $Br = [-2.0, 2.0]$ and $Le = [5.0, 10]$: (a) drag coefficient; (b) lift coefficient; (c) averaged Nusselt number and (d) averaged Sherwood number.

colored with the vorticity. The detailed setup of the parameters is presented in the caption of Fig. 17. It shows that the obtained streamlines and contours of the temperature and the species concentration match well with literature [53].

For the configuration (c) in Fig. 15(c), the following boundary conditions are imposed along the fluid boundaries.

- $u^* = U_\infty = 1.0;\ v^* = \theta = C = 0.0; \quad \forall \boldsymbol{x} \in \Gamma_{inlet}$
- $p^* = 0.0 \quad \forall \boldsymbol{x} \in \Gamma_{outlet}$
- $\boldsymbol{u}^* = 0.0;\ \frac{\partial \theta}{\partial \boldsymbol{n}} = \frac{\partial C}{\partial \boldsymbol{n}} = 0.0 \quad \forall \boldsymbol{x} \in \Gamma_w \cup \Gamma_e \cup \Gamma_n \cup \Gamma_s$
- $\boldsymbol{u}^* = 0.0;\ T = C = 1.0 \quad \forall \boldsymbol{x} \in \Gamma_{cyl}$

The Dirichlet boundary condition along the embedded interface, the dotted blue circle, is weakly satisfied by the Nitsche's method. The length of the enclosure is $L = 1.0$ and the diameter of cylinder is $0.4L$ in the configuration (c). There are about 60 elements along the cylinder's diameter. The total number of elements is 22 500. The time step taken is $d\tau = 0.01$. The obtained contours of the temperature and the species, and the streamlines are compared with literature [54] in Fig. 18. The contours in Fig. 18(d) are colored with the spanwise vorticity. This comparison shows a good agreement between the results obtained by the proposed numerical scheme and the well-validated results in literature [54].

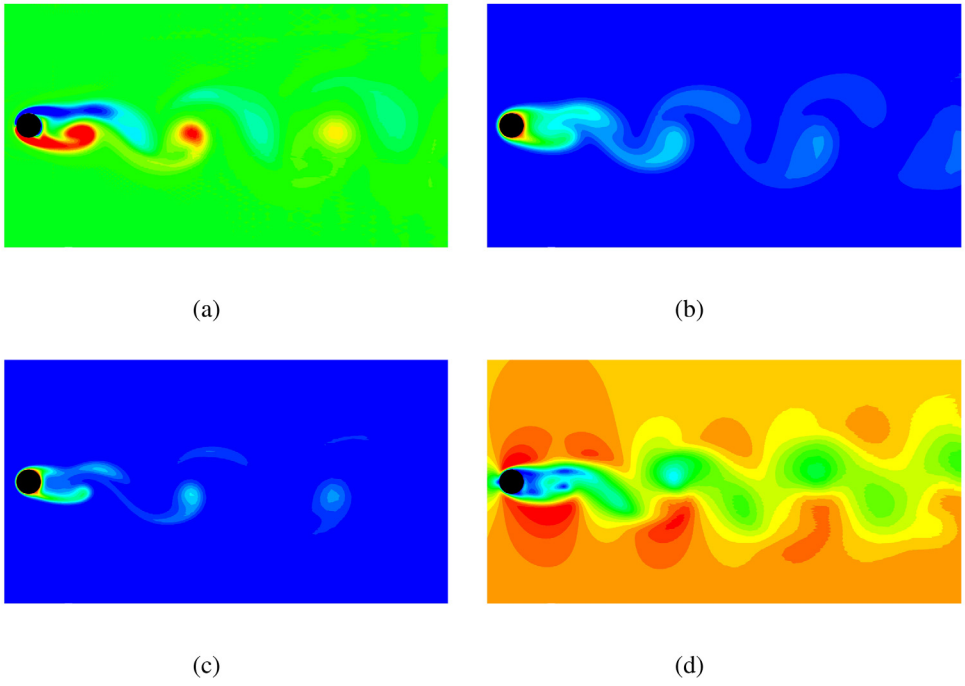

Fig. 22. Contours for double-diffusive mixed convection over a heated cylinder at $Re = 100$, $Pr = 0.7$, $Ri = 1.0$, $Br = -2.0$, $Le = 5.0$ and $\tau = 150$: (a) vorticity field ($\omega \in [-2.0, 2.0]$); (b) temperature field ($\theta \in [0.0, 1.0]$); (c) species field ($C \in [0.0, 1.0]$); and (d) velocity magnitude ($|\boldsymbol{u}^*| \in [0.0, 1.2]$).

4.2.2. Double-diffusive mixed convection over a rotating disk

The benchmark case of a rotating disk is frequently used to assess the robustness of the immersed boundary methods. In this case, an angular velocity $a = 1.0$ is weakly imposed along the embedded interface using the Nitsche's methods, as shown in Fig. 4(a). Hence the following boundary condition is imposed along the embedded interface, $\boldsymbol{u}^* = 0.0;\ \theta = C = 1.0;\ a = 1.0$. The freestream $U_\infty = 1.0;\ \theta = C = 0.0$ flows into the domain from the left and exits via the outlet. While the disk starts rotating in the counter-clockwise direction, a negative lift force is generated around the disk, as shown in Fig. 19. It is found that the obtained results of lift force for a rotating disk in forced convection ($Ri = 0.0$) match well with literature [24,55,56] in Fig. 19. Furthermore, it is also observed that the convection of the species also has a remarkable influence to the vortex dynamics in wake. Hence, it is believed that the proposed numerical scheme is robust for heat & mass transfer simulations involving strong velocity gradients. The corresponding contours of the vorticity, the temperature and the species behind a rotating disk are plotted in Fig. 20.

4.2.3. Heat and mass transfer over a heated cylinder

The performance of the proposed numerical scheme is also assessed in the case of double-diffusive mixed convection over a fixed heated cylinder. In this case, the following boundary conditions are imposed along the embedded interface using the Nitsche's methods, $\boldsymbol{u}^* = 0.0;\ \theta = C = 1.0$. The time step size is $d\tau = 0.01$. The time histories of the hydrodynamic forces, the averaged Nusselt number and the averaged Sherwood number are presented in Fig. 21. It is observed that the buoyancy ratio has a significant influence on the hydrodynamic and the thermal responses. The contours of the spanwise vorticity, the temperature, the species and the velocity magnitude for a fixed heated cylinder at $Re = 100$, $Pr = 0.7$, $Ri = 1.0$, $Br = -2.0$ and $Le = 5.0$ are plotted in Fig. 22.

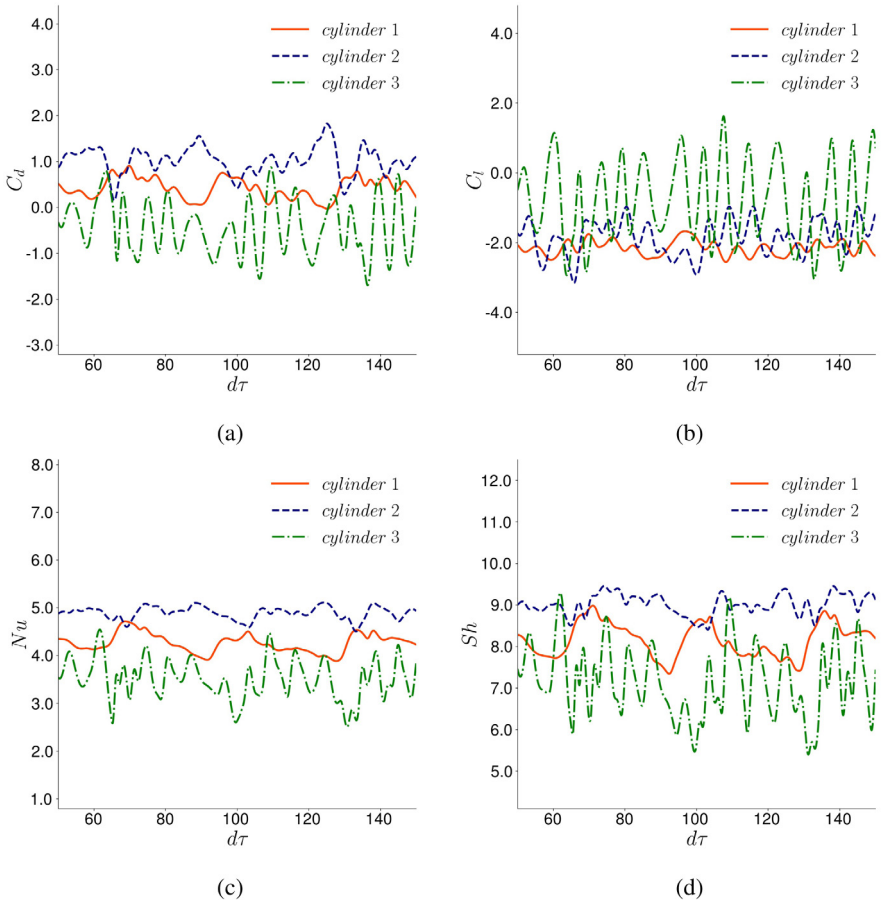

Fig. 23. Double-diffusive mixed convection over an equilateral-triangular arrangement at $Re = 100$, $Pr = 0.7$, $Ri = 1.0$, $Br = 1.0$, $Le = 5.0$ and $g^* = 3.0$: (a) drag coefficient; (b) lift coefficient; (c) averaged Nusselt number and (d) averaged Sherwood number.

4.2.4. Heat and mass transfer over an equilateral-triangular arrangement

In multi-body systems, e.g., side-by-side, tandem, staggered or arrays configurations, the interaction between the shear layers in wake is very complicated. To assess the robustness of the proposed numerical scheme, the heat & mass transfer over three heated cylinders in an equilateral-triangular arrangement at $Re = 100$, $Pr = 0.7$, $Br = 1.0$, $Le = 5.0$ and $g^* = 3.0$ is studied in this section. The time histories of the hydrodynamic forces, the averaged Nusselt number and the averaged Sherwood number are plotted in Fig. 23. It is found that the bottom cylinder downstream (cylinder 3) experiences the largest fluctuations in those cases. The contours of the spanwise vorticity, the temperature, the species and the velocity magnitude are presented in Fig. 24, where a large high-temperature region and a strong acceleration of fluid velocity are observed around the cylinder 3 in Figs. 24(b) and 24(d) respectively.

The proposed numerical scheme is further assessed for the case of vortex-induced vibrations of heated cylinders in an equilateral-triangular arrangement at $Re = 100$, $Pr = 0.7$, $Ri = 1.0$, $Br = 1.0$ and $Le = 5.0$. In this case, each cylinder is attached to a spring–damper system ($m^* = 10$, $\zeta = 0.01$ and $Ur = 6.0$). The time step size is $d\tau = 0.01$ and the total number of element is about 80 000. The time histories of the hydrodynamic forces, the averaged Nusselt number, the averaged Sherwood number, the streamwise vibration and the transverse vibration are shown in Fig. 25. Similar to the case of fixed cylinders in an equilateral-triangular arrangement in the last paragraph, the cylinder 3 experiences the largest fluctuation of the hydrodynamic forces, the heat & mass transfer and the vibration motion, because of the inefficiency in heat & mass transfer. The contours of the vorticity, the temperature, the species and

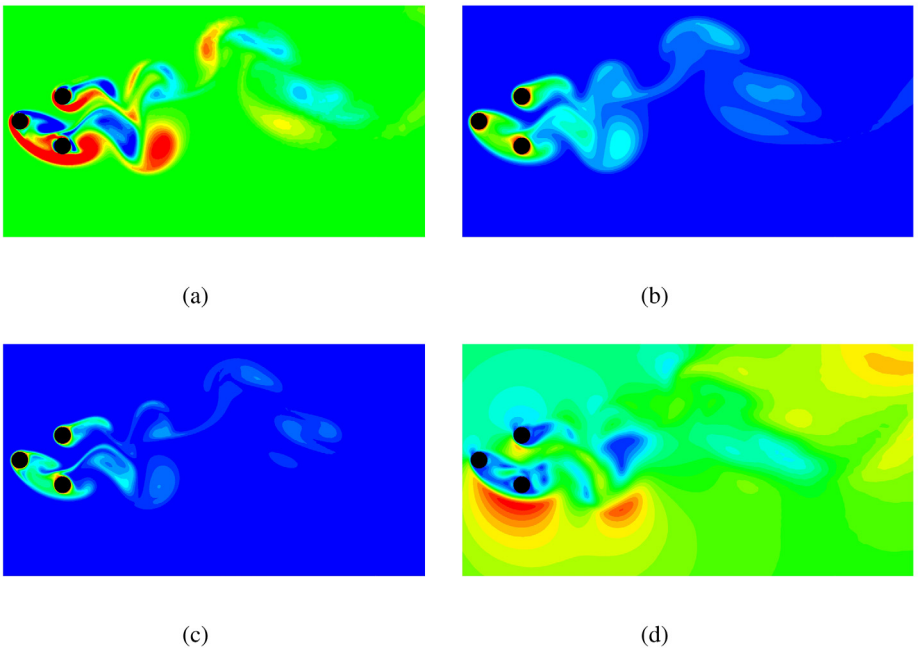

Fig. 24. Contours for double-diffusive mixed convection over an equilateral-triangular arrangement at $Re = 100$, $Pr = 0.7$, $Ri = 1.0$, $Br = 1.0$, $Le = 5.0$, $g^* = 3.0$ and $\tau = 100$: (a) vorticity field ($\omega \in [-2.0, 2.0]$); (b) temperature field ($\theta \in [0.0, 1.0]$); (c) species field ($C \in [0.0, 1.0]$) and (d) velocity magnitude ($|\boldsymbol{u}^*| \in [0.0, 2.2]$).

the velocity magnitude are presented in Fig. 26. It is believed that the proposed numerical formulation is robust and accurate for the simulation of complicated multi-physics and multi-scale simulations involving heat & mass transfer and fluid–structure interaction.

5. Conclusions

A Nitsche stabilized finite element method for heat & mass transfer and fluid–structure interaction was proposed in this study. The GLS/PSPG stabilization was employed to approximate the velocity and pressure fields using the same polynomial order. The nonlinear advection–diffusion equations were linearized using Newton procedures. The symmetric and non-symmetric Nitsche's methods were utilized for heat & mass transfer along embedded interface(s). An upwind term was included in Nitsche's methods to enhance the stability in case of fast moving interfaces across the background mesh. The jumps across the edges of the cut cells were minimized by the Ghost penalty method. The embedded discontinuous function within the cut cells was numerically integrated by the projection-based adaptive Gauss quadrature numerical integration scheme. The second-order accurate unconditionally stable generalized-α time integration was derived and implemented for heat & mass transfer. A second-order accurate staggered-partitioned weakly coupling fluid–structure coupling scheme was employed. The performance of the methodology was extensively tested for several benchmark examples, e.g., the flow over fixed/rotating/vibrating heated cylinder(s) in enclosure and external flow. The proposed numerical scheme was validated with the empirical correlation, experimental data and simulations in literature. All results obtained in the numerical examples were in excellent agreements with literature. Key advantages of the present methodology consisted of the robustness observed to efficiently deal with the large structural displacements, the strong thermal, species & velocity gradients and the intensive nonlinearity in boundary layer induced by heat & mass transfer. It accurately resolved the enhanced physics in multi-physics and multi-scale simulations involving heat & mass transfer and fluid–structure interaction.

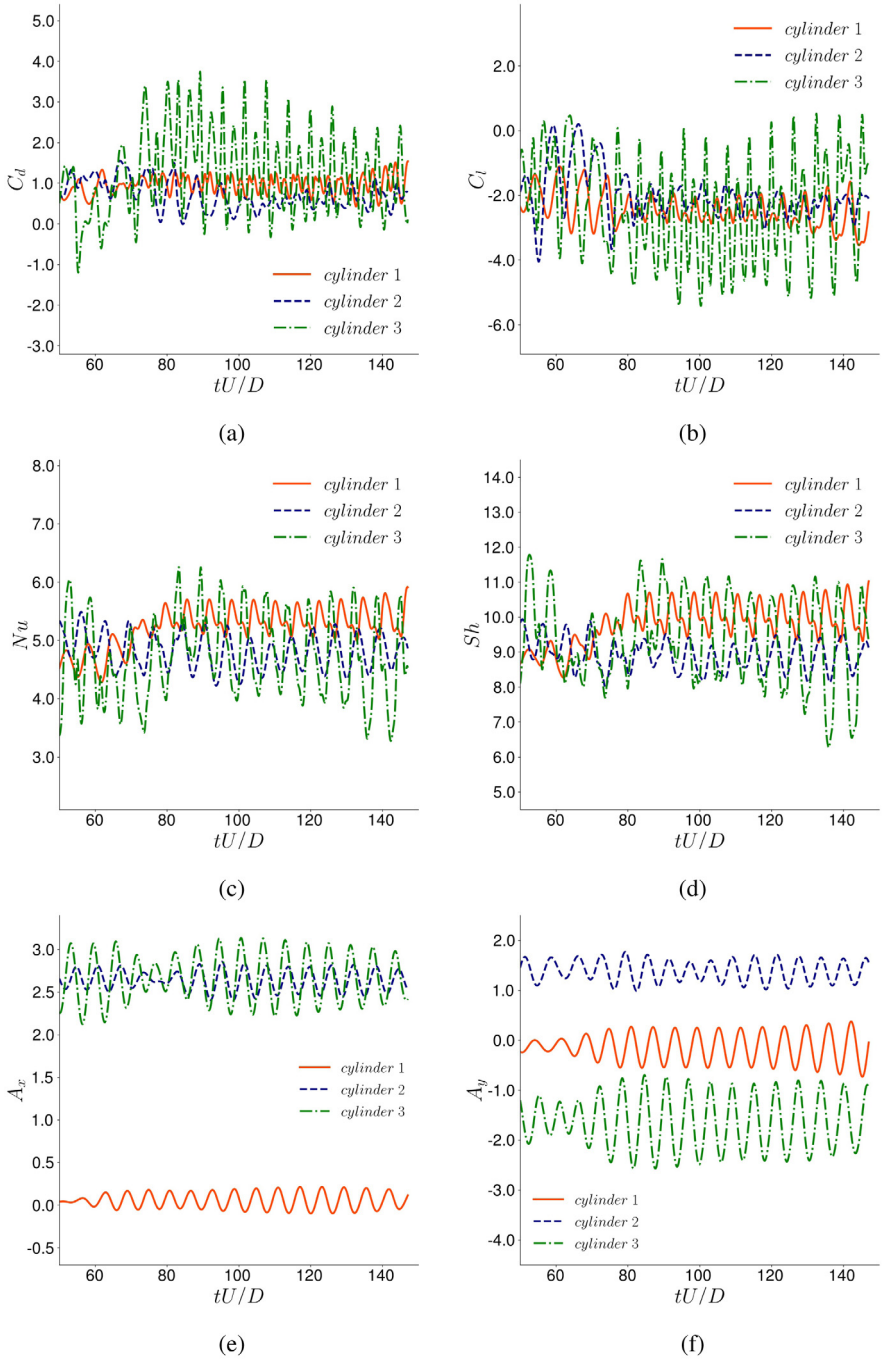

Fig. 25. Double-diffusive mixed convection over an equilateral-triangular arrangement at $Re = 100$, $Pr = 0.7$, $Ri = 1.0$, $Br = 1.0$, $Le = 5.0$, $g^* = 3.0$ and $Ur = 6.0$: (a) drag coefficient; (b) lift coefficient; (c) Nusselt number; (d) Sherwood number; (e) streamwise motion and (f) transverse motion.

Declaration of competing interest

The authors declare that they have no known competing financial interests or personal relationships that could have appeared to influence the work reported in this paper.

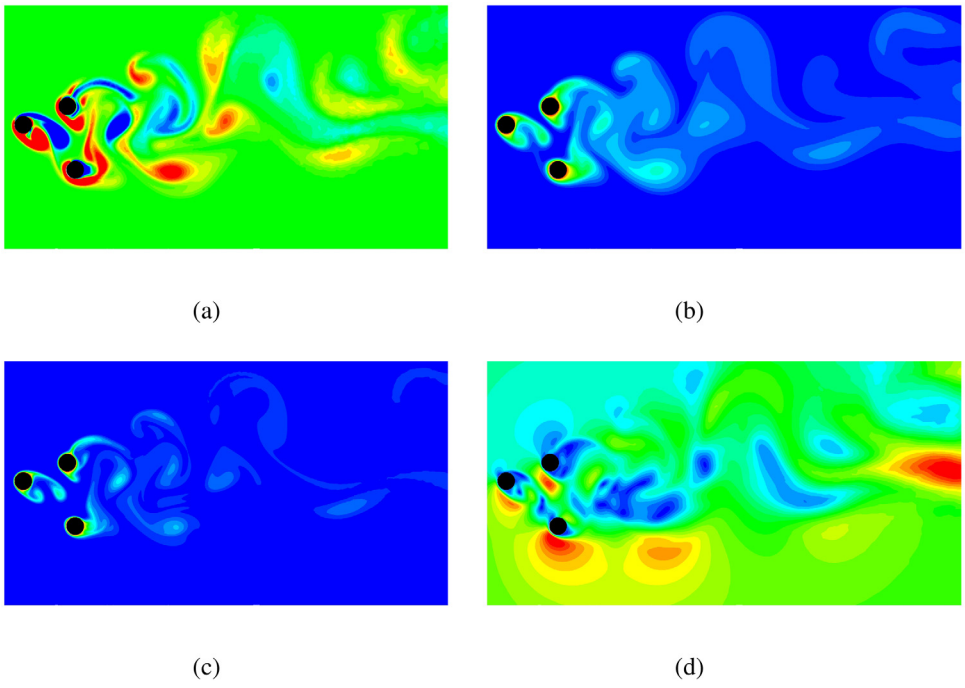

Fig. 26. Contours for double-diffusive mixed convection over an equilateral-triangular arrangement at $Re = 100$, $Pr = 0.7$, $Ri = 1.0$, $Br = 1.0$, $Le = 5.0$, $g^* = 3.0$, $Ur = 6.0$ and $\tau = 100$: (a) vorticity field ($\omega \in [-2.0, 2.0]$); (b) temperature field ($\theta \in [0.0, 1.0]$); (c) species field ($C \in [0.0, 1.0]$) and (d) velocity magnitude ($|\boldsymbol{u}^*| \in [0.0, 2.2]$).

References

[1] C.S. Peskin, Flow patterns around heart valves: a numerical method, J. Comput. Phys. 10 (2) (1972) 252–271.
[2] C.S. Peskin, Numerical analysis of blood flow in the heart, J. Comput. Phys. 25 (3) (1977) 220–252, http://dx.doi.org/10.1016/0021-9991(77)90100-0.
[3] C.S. Peskin, The immersed boundary method, Acta Numer. 11 (2002) 479–517, http://dx.doi.org/10.1017/S0962492902000077.
[4] L. Lee, R.J. LeVeque, An immersed interface method for incompressible Navier–Stokes equations, SIAM J. Sci. Comput. 25 (3) (2003) 832–856, http://dx.doi.org/10.1137/S1064827502414060.
[5] X. Wang, W.K. Liu, Extended immersed boundary method using FEM and RKPM, Comput. Methods Appl. Mech. Engrg. 193 (12–14) (2004) 1305–1321.
[6] R. Mittal, G. Iaccarino, Immersed boundary methods, Annu. Rev. Fluid Mech. 37 (2005) 239–261.
[7] C. Shu, N. Liu, Y.T. Chew, A novel immersed boundary velocity correction–lattice Boltzmann method and its application to simulate flow past a circular cylinder, J. Comput. Phys. 226 (2) (2007) 1607–1622.
[8] R. Glowinski, T.W. Pan, J. Periaux, A fictitious domain method for external incompressible viscous flow modeled by Navier-Stokes equations, Comput. Methods Appl. Mech. Engrg. 112 (1–4) (1994) 133–148.
[9] R. Glowinski, T.W. Pan, T.I. Hesla, D.D. Joseph, A distributed Lagrange multiplier/fictitious domain method for particulate flows, Int. J. Multiph. Flow. 25 (5) (1999) 755–794.
[10] R. Van Loon, P.D. Anderson, F.P. Baaijens, F.N. Van de Vosse, A three-dimensional fluid–structure interaction method for heart valve modelling, Comptes Rendus Mecanique 333 (12) (2005) 856–866.
[11] A. Gerstenberger, W.A. Wall, An extended finite element method/Lagrange multiplier based approach for fluid–structure interaction, Comput. Methods Appl. Mech. Engrg. 197 (19) (2008) 1699–1714.
[12] U.M. Mayer, A. Popp, A. Gerstenberger, W.A. Wall, 3D fluid–structure-contact interaction based on a combined XFEM FSI and dual mortar contact approach, Comput. Mech. 46 (1) (2010) 53–67.
[13] F. Alauzet, B. Fabrèges, M.A. Fernández, M. Landajuela, Nitsche-XFEM for the coupling of an incompressible fluid with immersed thin-walled structures, Comput. Methods Appl. Mech. Engrg. 301 (2016) 300–335.
[14] F. Brezzi, On the existence, uniqueness and approximation of saddle-point problems arising from Lagrangian multipliers, Rev. Fr. Autom. Inform. Rech. Oper. Analyse Num. 8 (R2) (1974) 129–151.
[15] F. Brezzi, K.J. Bathe, A discourse on the stability conditions for mixed finite element formulations, Comput. Methods Appl. Mech. Engrg. 82 (1–3) (1990) 27–57.

[16] J. Nitsche, Über ein Variationsprinzip zur Lösung von Dirichlet-Problemen bei Verwendung von Teilräumen, die keinen Randbedingungen unterworfen sind, in: Abhandlungen Aus Dem Mathematischen Seminar Der UniversitäT Hamburg, 36, (1) Springer, 1971, pp. 9–15.
[17] E. Burman, Ghost penalty, C. R. Math. 348 (21–22) (2010) 1217–1220.
[18] E. Burman, A penalty-free nonsymmetric Nitsche-type method for the weak imposition of boundary conditions, SIAM J. Numer. Anal. 50 (4) (2012) 1959–1981.
[19] D. Schillinger, I. Harari, M.C. Hsu, D. Kamensky, S.K. Stoter, Y. Yu, Y. Zhao, The non-symmetric Nitsche method for the parameter-free imposition of weak boundary and coupling conditions in immersed finite elements, Comput. Methods Appl. Mech. Engrg. 309 (2016) 625–652.
[20] Y. Bazilevs, M.-C. Hsu, M. Scott, Isogeometric fluid–structure interaction analysis with emphasis on non-matching discretizations, and with application to wind turbines, Comput. Methods Appl. Mech. Engrg. 249 (2012) 28–41.
[21] A. Massing, M.G. Larson, A. Logg, M.E. Rognes, A stabilized nitsche fictitious domain method for the Stokes problem, J. Sci. Comput. 61 (3) (2014) 604–628.
[22] L.H. Nguyen, S.K.F. Stoter, M. Ruess, M.A.S. Uribe, D. Schillinger, The diffuse Nitsche method: Dirichlet constraints on phase-field boundaries, Int. J. Numer. Methods Eng. 113 (4) (2018) 601–633.
[23] Z. Zou, W. Aquino, I. Harari, Nitsche's method for Helmholtz problems with embedded interfaces, Internat. J. Numer. Methods Engrg. 110 (7) (2017) 618–636.
[24] B. Liu, D. Tan, A nitsche stabilized finite element method for embedded interfaces: Application to fluid-structure interaction and rigid-body contact, J. Comput. Phys. (2020) 109461.
[25] E. Burman, P. Hansbo, Fictitious domain finite element methods using cut elements: II. a stabilized Nitsche method, Appl. Numer. Math. 62 (4) (2012) 328–341.
[26] W.G. Dettmer, C. Kadapa, D. Perić, A stabilised immersed boundary method on hierarchical b-spline grids, Comput. Methods Appl. Mech. Engrg. 311 (2016) 415–437.
[27] C. Kadapa, W.G. Dettmer, D. Perić, A stabilised immersed boundary method on hierarchical b-spline grids for fluid–rigid body interaction with solid–solid contact, Comput. Methods Appl. Mech. Engrg. 318 (2017) 242–269.
[28] C. Kadapa, W.G. Dettmer, D. Perić, A stabilised immersed framework on hierarchical b-spline grids for fluid-flexible structure interaction with solid–solid contact, Comput. Methods Appl. Mech. Engrg. 335 (2018) 472–489.
[29] Z. Chen, C. Shu, L.M. Yang, X. Zhao, N.Y. Liu, Immersed boundary–simplified thermal lattice Boltzmann method for incompressible thermal flows, Phys. Fluids 32 (1) (2020) 013605.
[30] G. Kefayati, An immersed boundary-lattice Boltzmann method for thermal and thermo-solutal problems of Newtonian and non-Newtonian fluids, Phys. Fluids 32 (7) (2020) 073103.
[31] T.J.R. Hughes, L.P. Franca, G.M. Hulbert, A new finite element formulation for computational fluid dynamics: VIII. The Galerkin/least-squares method for advective-diffusive equations, Comput. Methods Appl. Mech. Engrg. 73 (2) (1989) 173–189.
[32] T.J.R. Hughes, L.P. Franca, M. Balestra, A new finite element formulation for computational fluid dynamics: V. circumventing the Babuška-Brezzi condition: A stable Petrov-Galerkin formulation of the Stokes problem accommodating equal-order interpolations, Comput. Methods Appl. Mech. Engrg. 59 (1) (1986) 85–99.
[33] J.G. Heywood, R. Rannacher, S. Turek, Artificial boundaries and flux and pressure conditions for the incompressible Navier–Stokes equations, Internat. J. Numer. Methods Fluids 22 (5) (1996) 325–352.
[34] D.N. Arnold, F. Brezzi, B. Cockburn, L.D. Marini, Unified analysis of discontinuous Galerkin methods for elliptic problems, SIAM J. Numer. Anal. 39 (5) (2002) 1749–1779.
[35] J.N. Jomo, F. de Prenter, M. Elhaddad, D. D'Angella, C.V. Verhoosel, S. Kollmannsberger, J.S. Kirschke, V. Nübel, E. van Brummelen, E. Rank, Robust and parallel scalable iterative solutions for large-scale finite cell analyses, Finite Elem. Anal. Des. 163 (2019) 14–30.
[36] K.E. Jansen, C.H. Whiting, G.M. Hulbert, A generalized-α method for integrating the filtered Navier–Stokes equations with a stabilized finite element method, Comput. Methods Appl. Mech. Engrg. 190 (3) (2000) 305–319.
[37] J. Chung, G.M. Hulbert, A time integration algorithm for structural dynamics with improved numerical dissipation: the generalized-α method, J. Appl. Mech. 60 (2) (1993) 371–375.
[38] W.G. Dettmer, D. Perić, A new staggered scheme for fluid–structure interaction, Internat. J. Numer. Methods Engrg. 93 (1) (2013) 1–22.
[39] S.W. Churchill, M. Bernstein, A correlating equation for forced convection from gases and liquids to a circular cylinder in crossflow, 1977.
[40] G. Juncu, A numerical study of momentum and forced convection heat transfer around two tandem circular cylinders at low Reynolds numbers. Part II: Forced convection heat transfer, Int. J. Heat Mass Transfer 50 (19) (2007) 3799–3808,
[41] S. Sarkar, A. Dalal, G. Biswas, Unsteady wake dynamics and heat transfer in forced and mixed convection past a circular cylinder in cross flow for high Prandtl numbers, Int. J. Heat Mass Transfer 54 (15–16) (2011) 3536–3551.
[42] B. Liu, H. Zhu, Secondary lock-in of vortex-induced vibration and energy transfer characteristics of a vibrating cylinder subject to cross buoyancy, Phys. Fluids 33 (7) (2021) 073607.
[43] C. Liu, X. Zheng, C. Sung, Preconditioned multigrid methods for unsteady incompressible flows, J. Comput. Phys. 139 (1) (1998) 35–57.
[44] N. Mahir, Z. Altaç, Numerical investigation of convective heat transfer in unsteady flow past two cylinders in tandem arrangements, Int. J. Heat Fluid Flow 29 (5) (2008) 1309–1318.
[45] E. Izadpanah, Y. Amini, A. Ashouri, A comprehensive investigation of vortex induced vibration effects on the heat transfer from a circular cylinder, Int. J. Therm. Sci. 125 (2018) 405–418.

[46] S. Sarkar, A. Dalal, G. Biswas, Unsteady wake dynamics and heat transfer in forced and mixed convection past a circular cylinder in cross flow for high Prandtl numbers, Int. J. Heat Mass Transfer 54 (15–16) (2011) 3536–3551.
[47] E. Izadpanah, Y. Amini, A. Ashouri, A comprehensive investigation of vortex induced vibration effects on the heat transfer from a circular cylinder, Int. J. Therm. Sci. 125 (2018) 405–418.
[48] Z. Yang, L. Ding, L. Zhang, L. Yang, H. He, Two degrees of freedom flow-induced vibration and heat transfer of an isothermal cylinder, Int. J. Heat Mass Transfer 154 (2020) 119766.
[49] Y. Bao, D. Zhou, C. Huang, Numerical simulation of flow over three circular cylinders in equilateral arrangements at low Reynolds number by a second-order characteristic-based split finite element method, Comput. & Fluids 39 (5) (2010) 882–899.
[50] S. Zheng, W. Zhang, X. Lv, Numerical simulation of cross-flow around three equal diameter cylinders in an equilateral-triangular configuration at low Reynolds numbers, Comput. & Fluids 130 (2016) 94–108.
[51] W. Chen, C. Ji, M.M. Alam, J. Williams, D. Xu, Numerical simulations of flow past three circular cylinders in equilateral-triangular arrangements, J. Fluid Mech. 891 (2020) A14.
[52] J.A. Weaver, R. Viskanta, Natural convection in binary gases due to horizontal thermal and solutal gradients, J. Heat Transfer 113 (1) (1991) 141–147,
[53] M.A. Teamah, W.M. El-Maghlany, Numerical simulation of double-diffusive mixed convective flow in rectangular enclosure with insulated moving lid, Int. J. Therm. Sci. 49 (9) (2010) 1625–1638.
[54] H. Xu, R. Xiao, F. Karimi, M. Yang, Y. Zhang, Numerical study of double diffusive mixed convection around a heated cylinder in an enclosure, Int. J. Therm. Sci. 78 (2014) 169–181.
[55] Y.-M. Chen, Y.-R. Ou, A.J. Pearlstein, Development of the wake behind a circular cylinder impulsively started into rotatory and rectilinear motion, J. Fluid Mech. 253 (1993) 449–484, http://dx.doi.org/10.1017/S0022112093001867.
[56] S. Mittal, B. Kumar, Flow past a rotating cylinder, J. Fluid Mech. 476 (2003) 303–334.